

TEL AVIV UNIVERSITY



אוניברסיטת תל-אביב

RAYMOND AND BEVERLY SACKLER
FACULTY OF EXACT SCIENCES
SCHOOL OF PHYSICS & ASTRONOMY

הפקולטה למדעים מדוייקים
ע"ש ריימונד וברלי סאקלר
בית הספר לפיסיקה ואסטרונומיה

The Tel-Aviv Astronomical Variability Survey – TAVAS

THESIS SUBMITTED FOR THE M.Sc. DEGREE
AT TEL-AVIV UNIVERSITY
SCHOOL OF PHYSICS AND ASTRONOMY

by

Elinor Medezinski

This work was carried out under the supervision of
Prof. Dan Maoz

March 2005

Acknowledgments

I would like to thank my thesis advisor, Prof. Dan Maoz, who guided, supported, and inspired me throughout the project.

I am grateful to Eran Ofek, who is an integral part of TAVAS, for his patience, guidance, and numerous matlab and IRAF scripts. I thank Yiftah Lipkin, who taught me everything I know about computers, and showed endless measures of patience.

I would also like to thank my fellow students, some of which who took part in the project, and other who helped me in other ways – Assaf Horesh, Keren Sharon, Dovi Poznanski, Orly Gnat, David Polishook, Ofer Yaron, Avi Shporer, Omer Bromberg, Efi Huri, and Lukasz Wyrzykowski.

A special thanks goes to the Wise Observatory staff and observers – Assaf Bervald, John Dan, Haim Mendelson, Sami Ben-Gigi, Ezra Mashal, Friedel Loinger, and Shai Kaspi.

Contents

1	Introduction	1
1.1	Variability Surveys – Recent, Ongoing and Planned	2
1.1.1	Past surveys	2
1.1.2	Ongoing surveys	4
1.1.3	Future surveys	7
1.2	TAVAS Compared to Other Surveys	8
1.3	TAVAS Scientific Motivation	10
1.3.1	Supernovae	10
1.3.2	Quasars and AGNs	14
1.3.3	Planetary transits and eclipsing binaries	17
1.3.4	Accreting binaries	19
1.3.5	Lensed quasars	21
1.3.6	Asteroids	22
1.3.7	Serendipitous discoveries	22
2	The TAVAS Project	23
2.1	Instrumentation	23
2.2	SITe & Maala Characterization	25
2.2.1	The SITe CCD Camera	25
2.2.2	Maala Focal Reimager	29
2.3	Survey Strategy	34
2.4	Survey Fields	36
3	Data Reduction, Analysis, and Archiving	40
3.1	Data Reduction	42
3.2	The SQL database	50

3.2.1	Design of the TAVAS database	52
3.2.2	Searching the database	55
3.3	The Scheduling Algorithm	55
4	Current Status and Future Tasks	58
	References	63
A	Table of Fields	70
B	TAVAS Database Tables	77
B.1	Field Table	77
B.2	Image Table	77
B.3	Filter Table	79
B.4	Object Table	80
B.5	Phot Table	81

Abstract

Wide-field surveys using large area detectors on small telescopes can explore the still-largely unstudied time domain in astronomy. In this thesis, I describe the Tel-Aviv Astronomical Variability Survey (TAVAS), which is using the Wise 1-m telescope. TAVAS monitors to $R \sim 20$ mag about 150 deg^2 of the sky, spread over 300 Galactic and extragalactic fields, on short and long intervals, for a duration of two years. The survey is sensitive to a variety of transient and variable phenomena, including asteroids, cataclysmic variables, AGNs, extrasolar planetary transits, and supernovae. I present the survey strategy and the rationale and choice of target fields. I then describe the commissioning stages of the survey, the characterization of the instruments, and the solution of various hardware and software problems that were encountered. An automated scheduling, data reduction, analysis, and archiving pipeline has been developed, to enable fast and efficient data mining. This, in turn, will allow for real-time identification and follow-up of transient events. Observations have been taking place, reduced, and archived nightly. Preliminary results, efficiency measures, and conclusion from the survey are presented, demonstrating the promise of TAVAS. I conclude by outlining the remaining tasks.

Chapter 1

Introduction

Variability of celestial objects has been known for centuries, and dates back to ancient discoveries of bright supernovae and comets. Nevertheless, the area of variable and transient astronomical phenomena still has large unexplored regions, even at the bright end. Compared to efforts in the past decade that were focused on building large-aperture telescopes, observing to higher redshifts and to fainter limits, the temporal domain has received less attention (e.g., Paczynski 2001). In some parts of the spectrum, mainly the X-ray and γ -ray bands, the sky has been monitored for several decades. Examples are the BATSE experiment on the Compton Gamma-Ray Observatory (Harmon et al. 2004), the HETE mission (Ricker et al. 2003), and the recently launched Swift mission (Gehrels et al. 2004) that issue alerts to the community on variability on timescales from milliseconds to years. However, there are, as of yet, no such rapid discovery systems in the optical regime.

Optical variability is therefore an observational frontier, with extensive regions of parameter space left to be explored. It has been only since the 1990s that large-scale optical surveys have started monitoring the sky. Technical advances have allowed the construction of small automated telescopes, large-area CCDs, and high-end computational hardware, all at relatively low costs. Such systems conducting large-scale variability surveys can advance many areas of research. For instance, surveys for microlensing events toward the Magellanic Clouds and the Galactic Bulge by the MACHO, EROS and OGLE groups (described below) have contributed significantly to the understanding of dark

matter (Alcock et al. 2000; Ansari 2004; Udalski et al. 1997). The search for extrasolar planet transits is another new and active field, with the first planet transit detected in 1999 (Charbonneau et al. 2000; Henry et al. 2000). Supernova (SN) searches now cover the redshifts range $z = 0 - 1.5$ with surveys like High- z , ESSENCE and GOODS (Tonry et al. 2003; Mikaitis et al. 2004; Stogler et al. 2004). Some experiments are designed for the detection and follow-up of optical counterparts to gamma-ray bursts (GRBs). Asteroids and Near Earth Objects are being searched for by several groups, e.g., LINEAR (Stokes et al 2000). Many of these experiments have been carried out with small aperture, wide-field telescopes.

In the following section, I review in more detail the past, present and future optical variability surveys, limiting the discussion to surveys that have a limiting magnitude of 20 or above. In § 1.2, I present our survey, TAVAS, which is the subject of this thesis, and compare it with the other surveys presented in the first section. In § 1.3, I elaborate on the different variable phenomena that can be found in TAVAS, and make an assessment of the number of events we expect to detect for each type.

1.1 Variability Surveys – Recent, Ongoing and Planned

1.1.1 Past surveys

The first large optical variability surveys of the 1990s, all done with 1-m class telescopes, were mostly focused on searching for microlensing events, and therefore covered only specific areas of the sky – namely fields in the Local Group – with a high sampling frequency. The **MACHO** project (Alcock et al. 2000) was the pioneering microlensing survey, observing the Large Magellanic Cloud (LMC) and the Small Magellanic Cloud (SMC) in the years 1992-1999, using the 1.27-m telescope (reaching 21 mag) at Mount Stromlo Observatory in Australia. Their main goal was to constrain the amount of dark matter in the Galactic Halo in the form of Massive Astronomical Compact Halo Objects (MACHOs) via the use of microlensing events. Some 30 well sampled (twice a night) $42' \times 42'$ fields observed with eight $2k \times 2k$ pixel CCDs produced, in the end, a total of

13-17 microlensing events.

The **Optical Gravitational Lensing Experiment** (OGLE-I; Udalski et al. 1992; Udalski et al. 1994; Udalski et al. 1995; Udalski et al. 1997) was also a survey searching for dark matter by means of microlensing. The survey was conducted between 1992-1995, using the 1-m telescope at the Las Campanas Observatory in Chile, with a $2k \times 2k$ pixel CCD camera, and a field of view (FOV) of $15' \times 15'$. In the four observing seasons, about 20 fields in the Galactic Bulge were repeatedly observed (once to three times a night) to 20 mag, and a total of 19 microlensing events were detected. At times when the Galactic bulge was not visible other fields were monitored. In addition to microlensing events, many variable stars were discovered, e.g., numerous detached eclipsing binaries (Kaluzny et al. 1996).

EROS (Experience pour la Recherche d'Objets Sombres; Aubourg et al. 1993; Ansari 2004) started monitoring the LMC and the SMC in 1990, first with photographic plates, and then with a dedicated wide-field CCD mounted on the 40-cm telescope at La Silla Observatory, Chile. In July 1996, the group started a more extensive program – EROS-2 (Afonso et al. 2003), on the MARLY 1-m telescope also located at La Silla. Two mosaic $8 \times 2k \times 2k$ pixel CCD cameras imaging in two wide pass-bands gave a FOV of $0.7^\circ \times 1.4^\circ$. Observations continued 7 years until 2003. They targeted around 80 fields toward the LMC, 10 toward the SMC, and about 150 fields in the direction of the Galactic bulge, as well as 29 fields in the Galactic plane away from the bulge. Each field had, at the end, between 200-400 images. EROS-2 obtained almost 50 million light curves, and found about ~ 30 microlensing events. However, many other types of events were found, including about 60 SNe.

AGAPE (Andromeda Gravitational Amplification Pixel Experiment; Ansari et al. 1997) monitored M31 for microlensing events of stars blended with the general M31 population, a method called “pixel lensing”. The project observed six fields in M31, but only four were densely sampled (about once a night). In total they obtained 70 nights scattered between 1994 and 1996, on the 2-m Bernard Lyot telescope at Pic du Midi Observatory in

France, equipped with a focal reducer and a $2k \times 4k$ pixel CCD. The FOV was 4.5×4 and the total survey area was 14×10 . Other than variables (Ansari et al. 2004), the survey found no microlensing events, but showed the feasibility of pixel lensing, which was then adopted in future surveys (e.g. POINT-AGAPE; see Belokurov et al. 2005).

MEGA (Microlensing Exploration of the Galaxy and Andromeda; de Jong et al. 2004) monitored two fields of M31 of about 0.5 deg^2 between the years 1999-2002, using several telescopes - the 2.5-m Isaac Newton Telescope (INT) at La Palma, the KPNO 4-m, and the 1.3-m and 2.5-m telescopes of MDM Observatory. Results were published from the 160 observation nights done with the Wide Field Camera (WFC) on INT, which has four 2048×4100 chips, giving an FOV of 0.29 deg^2 . The two fields were monitored almost every night, among which about 100 epochs were useful. Some 14 microlensing events were detected in this survey, two of which were already known from POINT-AGAPE survey.

1.1.2 Ongoing surveys

Ongoing variability surveys, which will be reviewed below, are OGLE-III, the successor of OGLE, superMACHO, extending the work of MACHO, as well as ESSENCE, Palomar-Quest, FSVS, DLS, and CFHTLS.

OGLE-III (Udalski 2003) is the third phase of OGLE, using the new 1.3m Warsaw Telescope at Las Campanas, Chile, and a new eight chip 8192×8192 pixel CCD mosaic camera installed since 2001. The FOV is $35' \times 35'$. More than 200 million stars are observed regularly once every 1-3 nights. The fields in the direction of the Galactic bulge consist of 162 high priority fields, which are sampled once every 1-2 nights, and 105 low priority fields, which are less frequently observed. Another 40 fields are toward the SMC, and 116 are toward the LMC. A sophisticated data analysis and microlensing event alert system has been implemented (Udalski 2003). Though mainly alerting on microlensing events, the output now also includes planetary transit alerts.

superMACHO (Becker et al. 2004a) is the second generation implementation of the MACHO project. It is a 5-year microlensing survey of the LMC, at the Cerro Tololo Inter-American Observatory (CTIO) using the Blanco 4m telescope. The survey started at 2001 and will run through 2005, using a total of 150 half-nights. An eight chip 2k×4k pixel CCD mosaic gives a FOV of 0.33 deg². 68 LMC fields are being monitored every night, and thus a total of ~ 23 deg² are covered. The survey is sensitive to flux variations in stars as faint as 23 mag. In 2003, they detected about 10 microlensing events. Also, some 70 SNe were found.

The **ESSENCE** project (“Equation of State: SuperNovae trace Cosmic Expansion”; Smith et al. 2002) is a 5-year SN survey, aimed at finding 200 type-Ia SNe in an area of 8 square degrees, in order to constrain the properties of the dark energy. It is the complementary survey of the superMACHO survey, using the same system – the Blanco 4m with a wide-field CCD mosaic, and using the same nights – exploiting the first half of the superMACHO nights. They observe 25 fields in two sets, where a set is revisited every 4 nights. In the two years since the project began, a total of ~ 60 SNe have been found (Matheson et al. 2004).

The **Sloan Digital Sky Survey** (SDSS; York et al. 2000) is an imaging and spectroscopy survey that will eventually cover a quarter of the sky ($\sim 10,000$ deg²). The survey uses a dedicated 2.5-m telescope at Apache Point Observatory in New Mexico, with a 30×2048 × 2048 pixel CCD mosaic imaging array, drift-scanning six scan lines in five bands, amounting to a 1.4° wide strip, and two spectrographs. The survey began in 2000, and will continue for 5 years. The SDSS aims to obtain 10⁶ galaxy redshifts and 100,000 quasar redshifts. The survey will explore mostly the North Galactic Cap (NGC) with just single exposures, therefore not revealing any variability information there. However, when the NGC is not accessible (during September, October, and November) the SDSS observes the South Galactic Pole. In this region, the southern equatorial stripe (a double drift scan, 2.5 wide, 90 long) will be scanned 45 times in five years, with an interval of 20 days between scans during a season.

The **Faint Sky Variability Survey** (FSVS; Groot et al. 2003) is a study of overall optical and astrometric variability at faint magnitudes (17-25 mag). The main targets are close binaries, RR Lyrae, optical counterparts to GRBs, Kuiper Belt Objects (KBO), and Solar neighborhood objects. FSVS utilizes the WFC (four 4k×2k pixel CCDs giving a 0.29 deg² FOV) mounted on the 2.5-m INT at La Palma, covering in the survey a total area of ~ 23 deg² at mid and high Galactic latitudes. The basic observing unit is a week, during which a field is observed 15 to 25 times, on timescales varying from once every 10 minutes to a few days. The field is revisited after a year for long duration variability. The survey started in 1998 and is apparently completed. To date, no clear-cut results have been published from it.

The **Deep Lens Survey** (DLS; Wittman et al. 2002; Becker et al. 2004b) is a 5-year transient search, started at the end of 1999 and expected to be completed by March 2005. Conducted using the 4-m Blanco and Mayall telescopes (at Cerro Tololo and Kitt Peak observatories, respectively), the survey is undertaking deep multicolor imaging of seven $2^\circ \times 2^\circ$ fields chosen at high Galactic latitude to avoid bright stars and Galactic extinction. The CCD mosaic camera has a $35' \times 35'$ FOV, and each target field is divided into 3×3 subfields, each having roughly the mosaic-size. Typical exposure times are 600 seconds, reaching limiting magnitude of 24. Each subfield is observed a total of 20 times in each of the four filters, to reach ~ 28 mag in the combined images. Five dithered exposures per subfield/filter are taken before moving to the next subfield, therefore achieving sensitivity to variability timescales of ~ 1000 sec. In each run (lasting several days) a field is revisited in the second half of the run, probing timescales of days, and runs are scheduled a month apart, sampling timescales of months as well. To reach the required 20 exposures, the field is observed a year later as well. The survey's main goal is studying large scale structure through weak microlensing, but its sensitivity to all these timescales provides it with the ability to detect Solar System objects, SNe, and variable stars.

The Canada-France-Hawaii 3.6-m Telescope (CFHT) is being used to perform the **Legacy Survey** (Cuillandre 2004). Beginning in 2003, 450 nights of dark and gray

time spanning 5 years will be devoted to the survey, using the MegaPrime/MegaCam instrument, a $36 \times 2048 \times 4612$ pixel CCD camera with $1^\circ \times 1^\circ$ FOV. The CFHTLS is composed of three different surveys – a very wide shallow survey (“Very Wide”), a wide synoptic survey (“Wide”), and a deep synoptic survey (“Deep”). The Very Wide survey covers most of the ecliptic plane, with a total area of $1300 \times 1 \text{ deg}^2$ and about 2-4 epochs per field. This survey will reveal a large sample of Solar System objects, and will be useful for studies of Galactic stellar populations and structure, and large scale structure. The Wide survey is aimed at studying large scale structure through weak lensing and galaxy clustering. Three patches of $7^\circ \times 7^\circ$ (170 deg^2 total) will be monitored for moving objects and transient phenomena, in two phases – early in the survey, and three years later. The Deep survey covers 4 deg^2 in four fields, which are observed 3 nights a run with 5 runs a years for each field. It is aimed mainly at the detection and monitoring of as many as 2,000 type-Ia SNe, in search of dark energy parameters.

The **Palomar-QUEST** survey (PQ; Graham et al. 2004) is a major new survey (started in summer 2003) employing the Oschin Schmidt 1-m telescope at Palomar Observatory with the QUEST camera. The QUEST camera is the largest of its kind - a 112-CCD mosaic, giving a $4.6^\circ \times 3.6^\circ$ FOV. The survey is planned to repeatedly observe a third of the sky ($\sim 15,000 \text{ deg}^2$ between $-25^\circ < \delta < 30^\circ$) in 7 passbands. Working in drift-scan mode, it scans 500 deg^2 a night, separated by time intervals of days to months, with a typical limiting magnitude in a single pass of $I \sim 21 \text{ mag}$. Some of the science goals are high redshift quasars, strong gravitational lensing, SNe and gamma-ray bursts (GRBs), and near-Earth asteroids and trans-Neptunian objects. The Palomar-Quest survey is a precursor of the large synoptic surveys (LSST, see below) with virtual observatory (VO) technologies that will be implemented in the future.

1.1.3 Future surveys

In the future, even larger-scale optical surveys are planned, notably Pan-STARRS and LSST. **Pan-STARRS** (Kaiser et al. 2004) – the Panoramic Survey Telescope & Rapid

Response System – is a wide-field imaging facility designed to observe the entire sky visible from Hawaii (3π steradians) several times a month. Pan-STARRS will be composed of 4 telescopes of 1.8-m, each equipped with a CCD mosaic camera of $32\text{k}\times 32\text{k}$ pixels, having a 7 deg^2 FOV, and will cover $6,000\text{ deg}^2$ per night. With exposures of 30 to 60 seconds, Pan-STARRS will reach a limiting magnitude of 24, and will observe different fields with different timescales, varying from 10 minutes, to days and years. This survey is intended to find all kinds of optical transient and variable phenomena, from Solar System objects - NEOs, KBOs and asteroids, to SNe, GRBs, AGNs, and gravitational micro lensing.

The **Large Synoptic Survey Telescope** (LSST; Tyson 2002) is another ambitious project designed to survey the entire visible sky every 5 days for moving objects and transient optical objects. The instrumental design is an 8.4-m telescope with a 2.3 Gpixel camera, which will be constructed of a mosaic of either $1\text{k}\times 1\text{k}$ or $2\text{k}\times 2\text{k}$ pixel CCDs, recording a 7 deg^2 FOV. With such a large aperture, exposures as short as 10 seconds will be enough to reach limiting magnitude of 24. LSST will survey up to $14,000\text{ deg}^2$ three times per month (assuming 15 clear nights a month), and after several years $30,000\text{ deg}^2$ will be surveyed in multiple bands. The co-added images will reach 27 mag. The LSST is planned to see first light only in 2011; For Pan-STARRS, first light is scheduled for January 2006, with deployment of the full array within a further two years.

1.2 TAVAS Compared to Other Surveys

In this thesis, I will describe the motivation, rationale, design and construction of TAVAS, an astronomical variability survey at Wise Observatory. To put it in the context of the previous discussion, I will here briefly summarize the main features of TAVAS and will compare them to those of other surveys.

The **Tel-aviv Astronomical Variability Survey** (TAVAS) has been operational since January 2004. Using the 1-m telescope at the Wise observatory, with a focal reimager called Maala, TAVAS records in every image $0.8^\circ \times 0.6^\circ$ of the sky on a $4\text{k}\times 2\text{k}$ pixel CCD camera. TAVAS is a comprehensive variability survey, covering a total of 150 deg^2 ,

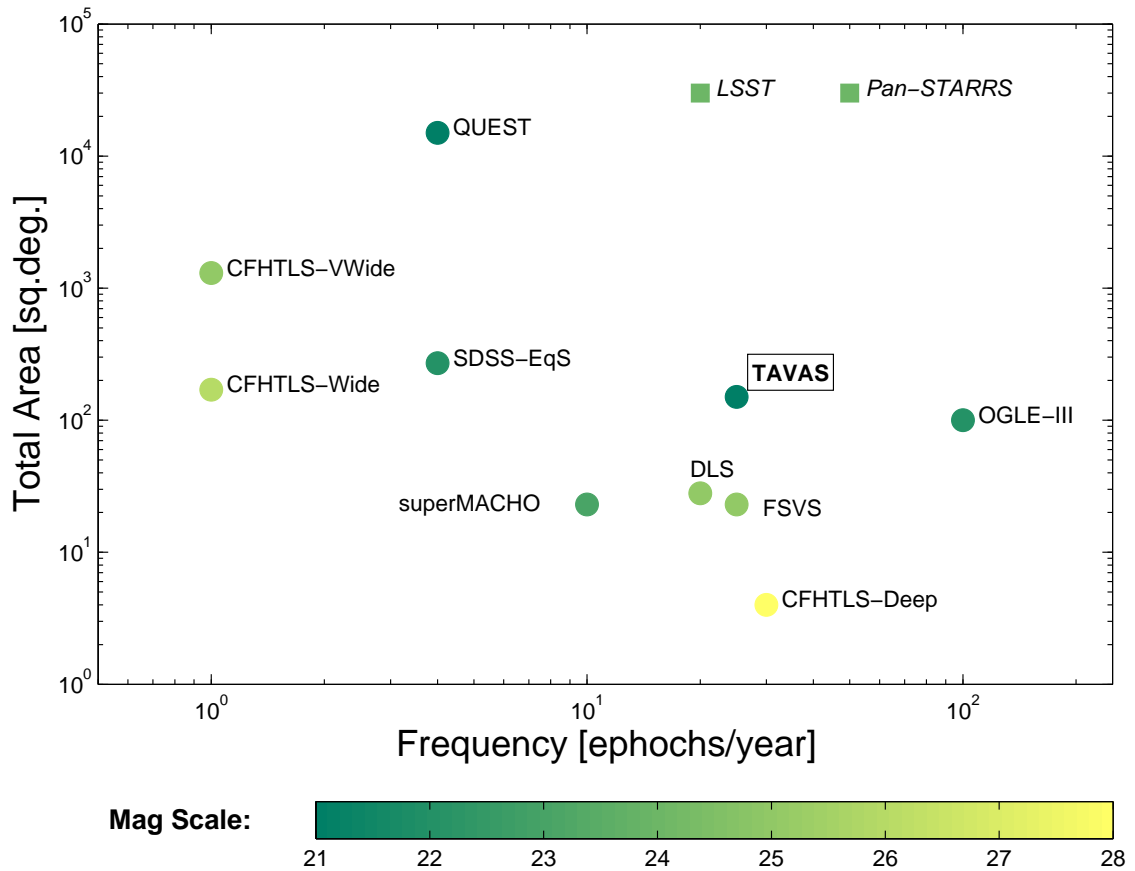


Fig. 1.1.– Comparison of TAVAS with current (circles) and future (squares) variability surveys, in terms of total area covered, sampling frequency, and depth.

over diverse timescales. All fields are re-observed after half an hour, some fields are also revisited every day, and some every couple of weeks. Fig. 1.1 shows a comparison in survey area, observation frequency and limiting magnitude of the on-going surveys (circles), the planned surveys (squares) described above, and TAVAS. TAVAS has a higher area and frequency combination, that establish it ahead of most other ongoing surveys. The OGLE-III experiment covers almost as much area of the sky with a higher sampling rate. However, since it is focused on microlensing events and planetary transits, OGLE-III searches only the LMC, SMC, and several Galactic plane fields, whereas TAVAS has fields spread over the entire sky (see Fig. 2.11 below for a field map). Palomar-QUEST

covers a much larger area than TAVAS, but it will only gather some 4 passes a year at each location, and with time intervals going down only to days, missing fast variables and moving objects. Since TAVAS samples every field twice a night, it will not overlook that population. To date, the PQ survey has observed $\sim 10,000 \text{ deg}^2$, of which about 7,000 deg^2 were observed twice. LSST and Pan-STARRS are by far more comprehensive than any other survey, but these surveys will begin only in several years. TAVAS is now well into its first year, and will achieve most of its goals by the time any of the future surveys begin observations.

1.3 TAVAS Scientific Motivation

Astronomical variability surveys that monitor large portions of the sky yield complete, systematic samples for studying variable phenomena. In the following subsections I present some of the scientific drivers of the TAVAS survey.

1.3.1 Supernovae

Supernovae (SNe) are explosions of stars, with a typical luminous energy release of order of 10^{49} erg, and brightness comparable for a brief period to that of an entire galaxy. Most of the optical radiation from such explosions is released on timescales of weeks. A supernova typically occurs once a century in a galaxy like the Milky way. SNe are classified, based on their explosion mechanisms, into two groups – type-Ia SNe, and core-collapse SNe. Type Ia SNe are believed to be explosions of white dwarfs accreting from, or merging with, binary companions, and reaching the Chandrasekhar mass. All other SNe are thought to arise from the core collapse of massive stars.

After an empirical correction for light-curve shape or decline rate, type-Ia SNe are observed to have a small dispersion in optical luminosity, making them useful as standard candles with which cosmological constants can be measured. The thermonuclear processes that occur in the progenitors of SNe, make SNe the main distributors of elements heavier than oxygen to the inter-stellar medium (ISM). SNe can also be used to study cosmic

star formation history (SFH). Core-collapse SNe follow SFH directly, since the massive members of a stellar population explode as SNe on timescales of millions of years, which are very short compared to cosmological timescales. SNe-Ia, on the other hand, occur only after a delay following the formation of a stellar population, during which their progenitors must evolve into white dwarfs and undergo binary evolution. If the delay time distribution is known, SNe-Ia can also be used to infer the SFH, with the advantage that, by the time the Ia's explode, dust associated with star formation has been dispersed, and thus SN-Ia-based SFHs should be less sensitive to extinction than UV-luminosity-based and core-collapse-based SFHs. Alternatively, by assuming a known SFH, one can use SN-Ia rates vs. cosmic time to deduce the delay time distribution, and discriminate between progenitor models of SNe Ia.

Star formation history and SN-Ia physics can also be studied by means of SN-Ia rates in galaxy clusters. Clusters are convenient places for this because they have a simple SFH (their current stellar population were formed at high z , and currently little star formation takes place) and because their deep potentials prevent escape of the metals accumulated over cosmic time. Furthermore, these metals are directly observable via their X-ray emission. Gal Yam et al. (2003) are conducting low and high redshift SN surveys in order to measure the SN-Ia rate in clusters. In a SN survey done at the Wise Observatory, Gal-Yam et al. found 14 SNe. Seven of those SNe were identified as type-Ia SNe in clusters at $0.06 < z < 0.2$, and are being used to calculate the SN rate at low redshift. Gal-Yam, Maoz, & Sharon (2002) used deep archival *Hubble Space Telescope* (HST) images to discover SNe and derive the cluster SN-Ia rate out to $z \sim 1$. Maoz & Gal-Yam (2004) used these measurements to obtain constraints on star formation in clusters and SN-Ia progenitor models, as shown in Fig. 1.2. The SN-Ia rate predictions are plotted for two stellar formation redshifts – $z = 2$ and $z = 3$, and for different time delay distributions between the formation of the stars in the cluster and explosion of some of them as SNe-Ia, normalized to agree with the measured iron abundance in clusters as observed in the X-rays (Mushotzky & Loewenstein 1997; White 2000). The

low measured rate in the high redshift bin sets a lower limit on stellar formation redshift, and an upper limit on the SN-Ia delay time. The short delay time ($\lesssim 2$ Gyr) also rules

Fig. 1.2.– Cluster SN-Ia rates vs redshift, derived from SNe found in archive HST images (points; Gal-Yam, Maoz & Sharon 2002), compared to predictions (curves) plotted for two stellar formation redshifts, $z = 2$ and $z = 3$, and for different time delay distributions. The models are normalized to agree with the observed iron mass in clusters. The left panel is a zoom-in on the right panel.

out some SN-Ia progenitor models, e.g., the “double degenerate” model, in which SNe-Ia form from white dwarf mergers. An alternative conclusion is that the iron was produced by other types of SNe, i.e., core collapse SNe. However, these core-collapse SNe would have necessarily originated from an ancient stellar population with top-heavy initial mass function (IMF). The high-mass stars that were formed together with the low-mass stars visible in clusters today, could not have produced the observed iron mass, given a normal IMF. A limiting factor in current studies is the small number of SN events available for the rate determination at each redshift. A major objective of TAVAS is to improve the accuracy of the cluster SN-Ia rate measurement at low z .

In TAVAS we monitor 119 galaxy clusters (see § 2.4) with redshifts $z < 0.12$. To estimate the number of cluster SNe-Ia that will be found, I assume Reiss’s (2000) SN-Ia rate measured in clusters at low-redshifts ($z = 0.06$), $R = 0.11^{+0.06}_{-0.07} h_{50}^2$ SNu, where 1 SNu = 1 SN century $^{-1}$ ($10^{10} L_{B\odot}$) $^{-1}$ and the Hubble parameter is $H_0 = h_{50} 50$ km s $^{-1}$ Mpc $^{-1}$. For a survey extent of two years, assuming an average cluster luminosity $3 \times 10^{12} L_{B\odot}$, a cluster visibility time of 6 months, a detection efficiency of 50%, and $H_0 = 70$ km s $^{-1}$ Mpc $^{-1}$, this gives about **40** SNe. From this sample, we will improve the accuracy of the measurement of the low- z cluster SN-Ia rate, which will help discriminate between different star-formation and time-delay models.

Gal-Yam et al. (2003) estimated the intergalactic stellar fraction in clusters to be 20^{+12}_{-15} percent, based on two SNe which had no apparent host galaxy, from the sample of seven cluster SNe described above. Some **12** of the 40 cluster SNe which will be detected by TAVAS are therefore expected to be intergalactic, and can be used to give a more accurate measurement of the intergalactic stellar fraction.

We further expect to detect with TAVAS \sim **340** field SNe (Sharon et al. 2005, in preparation) at $z \sim 0.1$, of which about 140 are SNe-Ia and 200 are core collapse. A uniform sample of nearby SNe is important in order to obtain a better estimate of the local field SN rate, which serves many applications – constraining models of star-formation histories, IMF evolution and dust extinction properties of SN hosts, as well as the typical

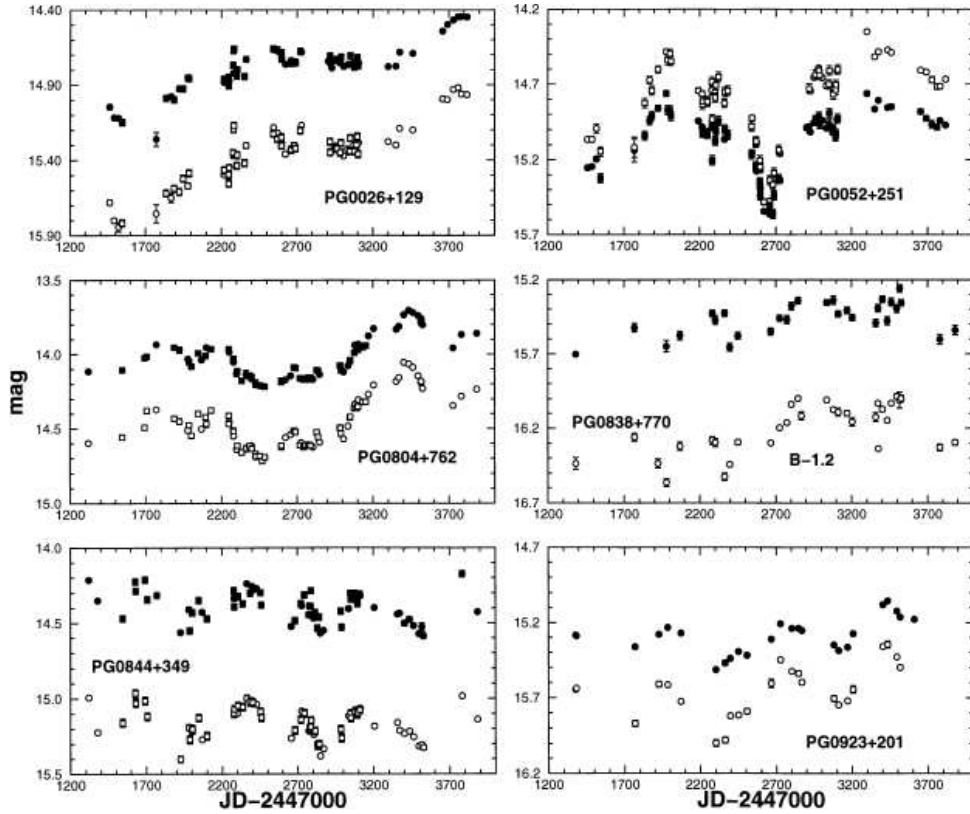


Fig. 1.3.– Six of the 42 low- z quasar light curves in B and R, taken at the Wise Observatory over 7 years by Giveon et al. (1999).

time delay for the explosion of SNe Ia. Moreover, from the sample of 200 core-collapse field SNe we expect to achieve a better knowledge of the progenitors and the physics of different SN types.

1.3.2 Quasars and AGNs

Active galactic nuclei (AGN) are characterized by luminous non-stellar emission from their central regions. The phenomena observed span all wavelength ranges, from the radio to gamma-rays, and include continuum and line emission, relativistic jets, and high velocity gas motions, based on the large widths of emission and absorption lines. In optical bands, AGN luminosities range from 10^{42} erg s $^{-1}$ (Seyfert galaxies) to 10^{47} erg s $^{-1}$ (the most

luminous quasars). AGN activity is believed to be caused by accretion onto supermassive black holes, by means of a surrounding accretion disk, in which the gravitational energy is converted to radiation. AGNs are variable, with optical fluctuations observed over timescales of weeks to years. The optical flux variations may be related to disk instabilities, or to inhomogeneities in the accretion flow. However, the accretion physics that power AGNs are poorly understood, let alone the causes of variability. Complete and well-sampled variability data could provide clues.

One of the best optical continuum AGN variability datasets was collected by Giveon et al. (1999) at the Wise Observatory, where 42 low- z quasars were monitored during seven years (see Fig. 1.3). The largest current samples of AGNs were produced by the 2dF QSO Redshift Survey (Croom et al. 2004 – 2×10^4 quasars), and by the SDSS (Vanden Berk et al. 2004 – of order $\sim 10^5$ quasars). In the SDSS, only two epochs, one spectroscopic and one photometric, per object were taken, therefore revealing limited variability information.

Giveon et al. (1999) measured the distribution of flux deviations about the mean for the quasars in their sample (see Fig. 1.4, top left). Using this distribution, I estimate for our survey, the probability as a function of magnitude, $P(m)$, of detecting at the 2σ level a quasar, based on its variability. The photometric accuracy of a typical TAVAS exposure is estimated from the signal to noise ratio (S/N) –

$$\frac{S}{N} = \frac{F_{ADU}}{\sqrt{F_{ADU} + Sky \cdot N_{pix}}} \cdot \sqrt{gain}, \quad (1.1)$$

where F_{ADU} are the source counts in analog-digital units (ADUs), Sky is the average background, and N_{pix} is the number of pixels in the aperture. The error is thus (see Fig. 1.4, top right) –

$$\sigma = \left(\frac{S}{N}\right)^{-1} + 0.03, \quad (1.2)$$

where 3% is a conservative estimate of the systematic photometric error. Integrating over magnitude the quasar number surface density per magnitude bin, $n_{qso}(m)$, (Hartwick & Schade 1990; see Fig. 1.4, bottom), weighted by the probability of detection in at least

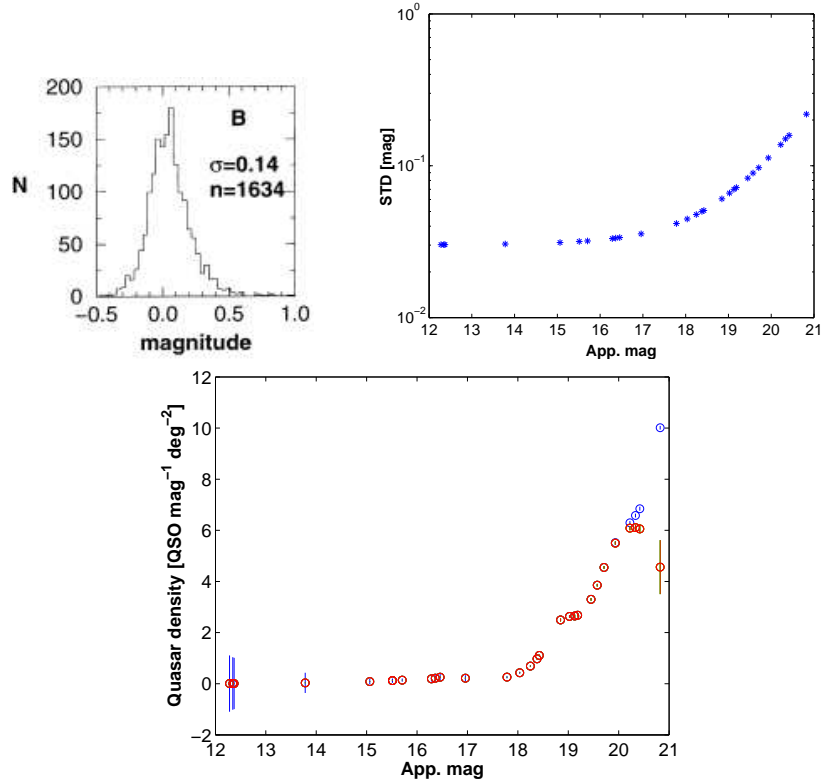


Fig. 1.4.– Quasar number estimates. *Top left*: Distribution of the flux deviations about the mean light curve level of the B measurements for the entire Giveon et al. (1999) quasar sample. *Top right*: Estimation of TAVAS photometric STD, measured in a typical image on the night of January 15, 2005. *Bottom*: Quasar density as function of apparent magnitude, as taken from Hartwick & Schade (1990) (blue points), and after the detection efficiency, determined from the first two figures, is taken into account (red points). Integrating this density (red points) over the magnitude range, gives the expected number of 1,200 quasars in 110 deg^2 .

one of 20 epochs

$$N_{qso} = 110 \cdot \int_{12}^{21} n_{qso}(m) [1 - (1 - P(m))^{20}] dm = 1200. \quad (1.3)$$

Thus, I estimate that in 110 deg^2 of intergalactic fields we will detect with TAVAS about **1,200** quasars at 20 epochs. For the quasars that will be found in the deep survey fields (about 20% of the fields; see § 2.4) we will have spectral and redshift information, and we expect that most of them will be at $z \sim 1 - 2$ (Croom et al. 2004). Such a sample of

1,200 quasars with some 20 epochs per quasar will constitute the largest, best-sampled, quasar variability dataset, having 10 times the epoch number of SDSS, and 30 times more objects than studied by Giveon et al. (1999).

1.3.3 Planetary transits and eclipsing binaries

Planets have masses lower than $\sim 10^{-2}M_{\odot}$, and luminosities in the range of $10^{-6} - 10^{-10}L_{\odot}$. These parameters make the direct detection of planets difficult. The available detection methods include: (1) displacement in frequency of spectral lines, or pulsar timing, corresponding to periodic Doppler-shift variations of the radial velocity of the primary star due to the planet; (2) periodic positional shifts of the star around the center of mass of the binary system; (3) direct detection of the reflected light from the planet; (4) periodic dimming in the star's luminosity due to a transit of a planet over the stellar disc; (5) deviations from the light curve of a point-mass lens, when a star+planet system gravitationally lenses a background star.

The first planetary system detected was found by pulsar timing measurements of PSR 1257+12 by Wolszczan & Frail (1992). This is a system of two few-earth-mass planets orbiting a pulsar. However, the greatest interest is in finding a **solar**-like planetary system, one which could perhaps harbor life. The first extrasolar planet around a solar-type star – 51 Pegasi – was discovered by Mayor & Queloz (1995), using the method of radial velocities determined from Doppler shifts of stellar absorption lines. High-precision radial velocity measurements have yielded over 100 planets in the past decade, with masses in the range $0.11 - 17 M_J$ ¹.

The first **transiting** giant planet was discovered orbiting HD209458 (Charbonneau et al. 2000; Henry et al. 2000), a system known previously from radial velocity measurements (see Fig. 1.5). Radial velocity observations could only provide a lower limit on the planetary mass, since the inclination of the orbit was unknown. However, combined with the new information from the transiting event the actual mass could be deduced

¹See <http://www.obspm.fr/encycl/encycl.html> for an updated list of extrasolar planets and the method of their discovery.

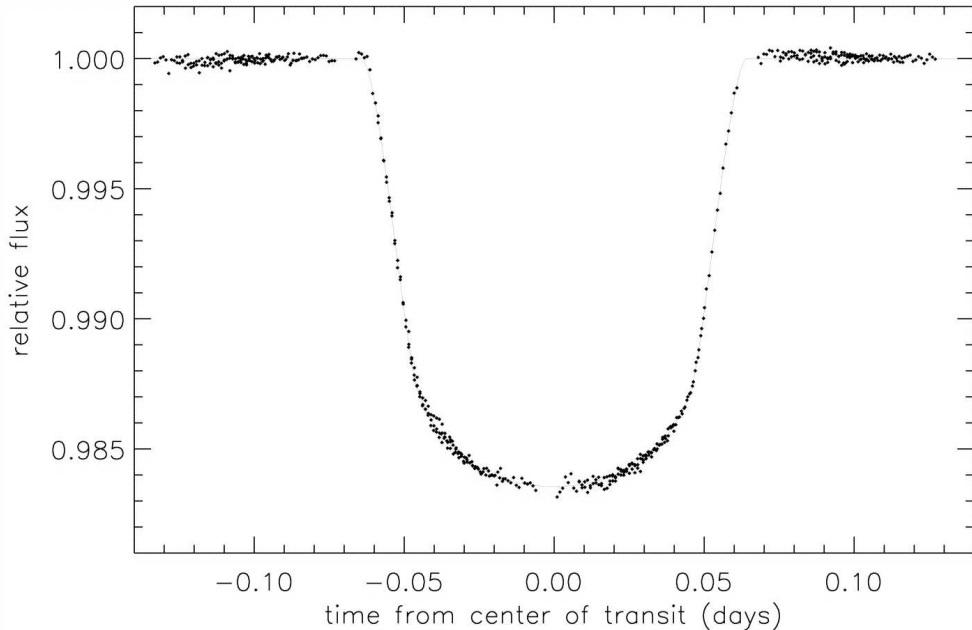


Fig. 1.5.— Phased light curve of HD209458, with a planetary orbital period of 3.52474 days (Brown et al. 2001).

for the first time, along with other parameters inferable from the transit - an estimate of the projected area, and therefore the radius (Mazeh et al. 2000) and density. Follow-up observations with HST even detected spectral absorption features from the planet’s atmosphere (Charbonneau et al. 2002; Vidal-Madjar et al. 2003).

The case of HD209458 motivated a number of new transit searches (see Horne 2003 for an overview)². The most successful of these has been the OGLE-III project, which has found some 180 candidates (Udalski et al. 2002abc, 2003, 2004) in the Galactic disk, having ~ 1000 epochs per candidate. Five of those systems have recently been confirmed to be planets by follow-up spectroscopy (Konacki et al. 2003, 2004ab; Bouchy et al. 2004; Pont et al. 2004).

Based on simulations (see § 2.3), we expect to find with TAVAS **8** true planetary transits of late-type stars in our Galactic fields, more than doubling the number of known

²The Web page <http://star-www.st-and.ac.uk/~kdh1/transits/table.html> gives an updated list with links to the experiments.

planetary transit systems.

An important byproduct of the transit search in the Galactic fields will be the detection of hundreds of eclipsing binaries. Detached eclipsing binaries are important in constructing models of stellar structure and stellar evolution (Lastennet & Valls-Gabaud 2002). In particular, eclipsing double-lined spectroscopic binaries provide the most accurate determination of stellar mass, radius, temperature and distance-independent luminosity for each of the components (Andersen 1991). While for $1 - 10 M_{\odot}$ main sequence stars these models are reasonably constrained, for the lower main sequence this is not the case, as they are usually fainter and harder to study. For decades, only two double-lined eclipsing binary systems with M-dwarf primaries have been known (Lacy 1977; Bopp 1974), with a few recent additions of such systems (e.g., Delfosse et al. 1999; Maceroni & Rucinski 1999). Finding even a few more with TAVAS will greatly enlarge this population.

In addition, TAVAS will reveal many short-period binaries (< 10 days), and will provide a large sample on which to base the period and mass distribution statistic, of a population that is not well characterized. Short period binaries are the progenitors of cataclysmic variables, SNe-Ia, and some X-ray binaries. Studying the properties and statistics of short-period binaries is therefore a step toward understanding the evolution of such stellar systems.

1.3.4 Accreting binaries

High-mass X-ray binaries (HMXB) are systems where an X-ray source – a neutron star or black hole, is accreting from a massive OB-type companion. The bright X-ray emission results from the accretion of matter from the early-type star. Some of these HMXB systems have shown evolution of their light curve, with very stable long-term modulation of hundreds of days (e.g. Alcock et al. 2001; McGowan & Charles 2003), quite larger than their orbital periods which are only several days long. This periodic variability is suspected to arise from changes in the accretion disk, and can therefore be indicative of the physical evolution of the system (see review in Charles & Coe 2003). Moreover, orbital

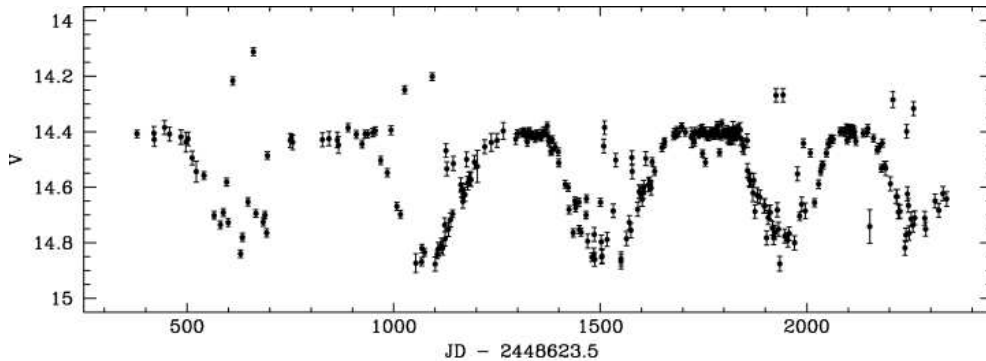


Fig. 1.6.— The 5.5 yr V -band light curve of the recurrent Be/X-ray transient A0538-66 (from MACHO project observations, showing a long-term modulation at $P=420.8$ d, where its calculated orbital period is 16.6d (Alcock et al. 2001).

parameters such as the system’s inclination and mass ratio can be determined from the light curves.

Comprehensive databases giving long-term optical light curves of HMXBs have been collected only by OGLE and MACHO, who surveyed primarily the LMC and SMC (see Fig. 1.6). In TAVAS, we are monitoring HMXBs in the Milky Way, for which this information does not exist.

Novae, which are one type of cataclysmic variables (CVs), are short orbital period (< 1 day) binaries, in which a main sequence star is transferring mass to its white dwarf companion. Novae have a bright nuclear eruption (of order 10 magnitudes), every $10^4 - 10^5$ years, due to ignition of the hydrogen accumulated on the white dwarf surface. Such a long period is obviously based on theoretical estimates alone. CVs in general, and novae in particular, serve as an observational ground for studying accretion processes, and are also an important source of elements to the ISM. Time series of novae have been gathered over the past years at Wise (Lipkin et al. 2001), and this will continue in the framework of TAVAS.

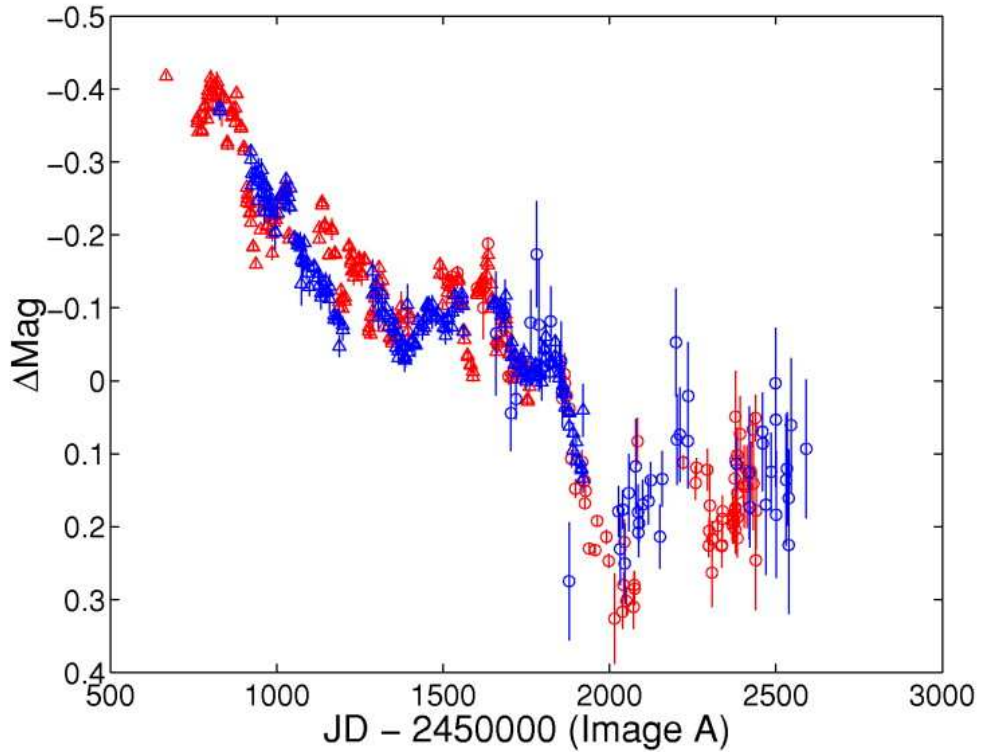


Fig. 1.7.– Light curve of two images of the gravitationally lensed quasar HE 1104 1805 – image A (red circles & triangles), overlaid by the best-fitting slope-corrected and time-delay shifted light curve of image B (blue circles & triangles) (from Ofek & Maoz 2003).

1.3.5 Lensed quasars

The light from about 1% of all bright quasars is gravitationally lensed into multiple images by an intervening galaxy. By measuring the time delay between the different images, one can measure the Hubble parameter H_0 , and constrain the mass distribution of the lens galaxy (Kochanek 2004). Monitoring of such systems has been part of a current study done at Wise (Ofek & Maoz 2003; see Fig. 1.7), and data accumulation is continued within TAVAS, where about **50** lensed quasar fields are being monitored.

1.3.6 Asteroids

A number of programs currently detect and characterize asteroids and comets in the Solar System, and also alert on possible hazardous impacts of Near-Earth Objects (NEOs) (LINEAR, Stokes et al. 2000; NEAT, Pravdo et al. 1999). We expect to find **thousands** of asteroids in TAVAS fields, and the data accumulated so far has shown that there are typically several such objects in each field. A population that will be specifically sought is the inner Earth-orbit asteroids, also known as Atens, that lie in orbits between the Sun and the Earth (Michel et al. 2000). This population of NEOs is poorly studied, since its members are hard to detect.

1.3.7 Serendipitous discoveries

Previous astronomical projects have shown that often when some characteristic of an experiment improves by an order of magnitude, new, unexpected discoveries are made. In our survey, new regions of parameter space will be explored, in terms of the combination of sampling rate, survey area, magnitude range, and duration. This will likely lead to the discovery of unexpected new phenomena.

Chapter 2

The TAVAS Project

The Tel-Aviv Astronomical Variability Survey (TAVAS) is an ongoing survey, planned to run for 2-3 years. For this survey, specific instruments were designed and built, and a comprehensive plan was laid out. In this chapter, I present a detailed description of the project. I discuss the instruments in § 2.1, the observational strategy in § 2.3, and the target fields in § 2.4.

2.1 Instrumentation

TAVAS is carried out using the 1-m telescope at the Wise Observatory. The observatory is located near Mitzpe-Ramon, 200 km south of Tel-Aviv. The site has poor seeing (2-3 arcsec), but is fairly dark, and has a large fraction of clear nights, making it particularly suitable for long-term monitoring surveys. Several successful monitoring projects have been conducted in the past using the Wise observatory (e.g., Giveon et al. 1999; Kaspi et al. 2000; Gal-Yam et al. 2003).

TAVAS utilizes Maala, a wide-field focal reimager designed especially for this purpose. Maala attaches to the Cassegrain f/7 focus of the telescope. It is built out of a set of 14 large lenses that collimate the telescope's beam, and refocus it at the other end, producing an f/3.05 beam at the new image plane (see Fig. 2.1 for Maala's optical layout).

The image is focused onto a back-illuminated 4096×2048 -pixel SITE CCD camera which has a pixel size of $15 \mu\text{m}$. The resulting image scale is $0.994 \text{ arcsec pixel}^{-1}$. The long

dimension is therefore 1.13° . Maala, due to its optical design, introduces some distortions at the edges of the large field of view. In TAVAS, a chip section of only 3000×2048 pixels, where the distortions are less dominant, is read out (see § 2.2.2, below). This gives an image area of almost 0.5 deg^2 in less readout time, and the readout time saved can be used to observe additional fields at better image quality.

The Wise observatory is linked through a microwave and fiber optic connection to Tel-Aviv University, allowing remote operation and fast data transfer. Due to its large

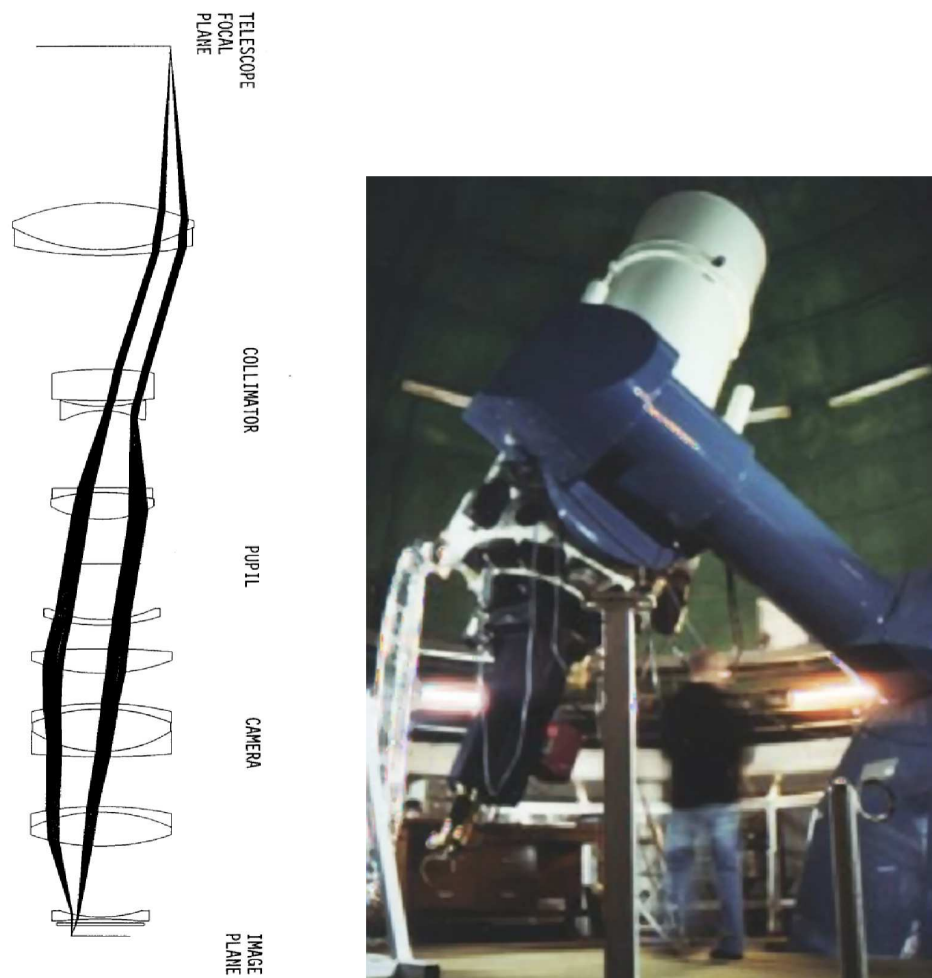


Fig. 2.1.– Left: Maala optical design. Right: Maala (black cylinder) attached to the telescope (white) at one end, and to the SITe CCD camera (Golden) at the other end.

physical length, Maala can collide with the telescope pier when the telescope is pointed east of the meridian and to declinations $\delta \gtrsim 65^\circ$. To prevent this, the telescope is restricted to point only up to a declination of $+55^\circ$, by hardware and software safety triggers (see § 2.2.2, below). However, additional testing and fine-tuning of the entire system are required before remote use of the telescope with Maala is allowed. Currently, all observations are done with an observer physically present at the observatory.

2.2 SITE & Maala Characterization

Maala saw first light on November 26, 2002. Since then, Maala and the SITE CCD camera have been subject to tests, aimed at determining the system's best working mode. Following is a review of the characterization and of the problems that we encountered and solved during the process of commissioning and working with the instruments.

2.2.1 The SITE CCD Camera



Fig. 2.2.– Maala first light image of the Moon, illustrating the large (0.5 deg^2) field of view.

a. Gain and readout noise The “gain” of the CCD, i.e., the ratio of photoelectrons to ADUs is controlled in the CCD’s operating software by a parameter called “gainDL”. The first task was to measure the gain and readnoise of the SITE as a function of gainDL. This was done on the night of November 24, 2002, by taking two bias-subtracted flat-field images, and dividing them. The standard deviation of counts in the resultant image (measured in areas with no cosmic rays, bad pixels or other artificial pixel values, which would corrupt the estimate), is used to calculate the gain as follows –

$$\sigma_{ADU}^2 \cdot gain^2 = 2N_{ADU} \cdot gain + 4(R.N._{ADU} \cdot gain)^2, \quad (2.1)$$

where N_{ADU} is the median pixel level, and $R.N._{ADU}$ (the readnoise in ADU) is calculated from the STD $\sigma_{B_1-B_2}$ in the difference of two bias images, using the relation –

$$R.N._{ADU} = \frac{\sigma_{B_1-B_2}}{\sqrt{2}}. \quad (2.2)$$

Thus,

$$gain = \frac{2N_{ADU}}{\sigma_{ADU}^2 - 4(R.N._{ADU})^2} = \frac{2N_{ADU}}{\sigma_{ADU}^2 - 2\sigma_{B_1-B_2}^2}. \quad (2.3)$$

The results are presented in the two plots in Fig. 2.2.1. Based on these results, we decided to set the system to a gainDL of 5, to get a corresponding gain of ~ 5 electrons/ADU and readnoise of 12 electrons. The saturation level with this gain setting is around 22,000 counts.

b. Photometric zero-point and linearity Standard fields were observed on January 15, 2005, and a photometric solution was calculated using the meastan routine written by D. Maoz. This routine is used to identify Landolt standard stars, and measure their instrumental magnitudes in the images. By comparing them to the known apparent

gain_vs_gainDL.eps RN_vs_gainDL.eps

Fig. 2.3.– *Left:* SITE gain for different settings of the gainDL parameter; *Right:* SITE readout noise vs. gainDL.

magnitude measured by Landolt (1992), it finds the photometric solution for the given night, i.e., a zero-point, an extinction coefficient, and a color term. Fig. 2.4 displays the calculated apparent magnitude vs. the Landolt V magnitude of the standard stars. The $\chi^2 \sim 1$, showing a good linear fit, demonstrates the linearity of the CCD response, where the peak pixels in the brightest star reach 82% of saturation. The count rate in an

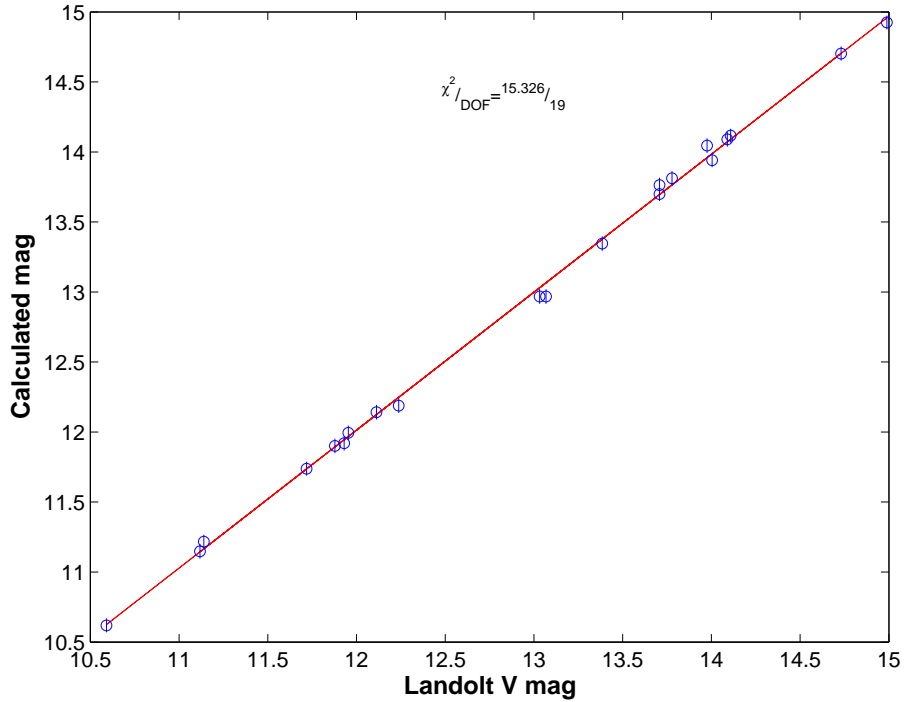


Fig. 2.4.– Calculated mag vs. Landolt mag, as measured in Standard fields, taken on the night of January 15th, 2005. These fields are used to determine the photometric zero-point, and to test the system linearity.

unfiltered exposure and the magnitude of a star, with color $V - R$, observed at airmass $A.M.$ are related by

$$V = -2.5 \log\left(\frac{\text{counts}}{\text{sec}}\right) + 23.26 - 0.21 \times A.M. + 0.95 \times (V - R) \quad (2.4)$$

for the V-band, or

$$R = -2.5 \log\left(\frac{\text{counts}}{\text{sec}}\right) + 23.26 - 0.21 \times A.M. - 0.04 \times (V - R) \quad (2.5)$$

for the R-band. The small color term for the R solution means that reliable R -band magnitudes can be estimated based on unfiltered TAVAS measurements.

c. Amplifiers and readout time The SITE has 2 on-chip amplifiers, that can be used individually or combined to read out the CCD. When working with both, one (L) reads the left half of the CCD (columns 1-1024), and the other (R) reads the right half (columns 1025-2048). Working in R+L mode reduces the readout time. On July 26, 2003 the readout time as a function of size of the region of the CCD read, was measured for the right amplifier only. The results, as presented in Fig. 2.5, show that when changing the size of the CCD's long axis, the readout time change as –

$$T_{Readout} = 192x + 37, \quad (2.6)$$

where x is the fraction of the CCD read out, and when changing the size of the short axis, this relation changes to –

$$T_{Readout} = 141x + 85. \quad (2.7)$$

The left amplifier had shown in the past high noise levels, and was therefore initially not used or tested. On October 22, 2003, we re-examined the left amplifier's noise levels, and found them to be acceptable. The readout mode was set to two amplifiers, giving a readout time shorter by a full minute. This worked well for the duration of about 7 months, from January to July, 2004. However, on the night of July 13, 2004, the left amplifier once again introduced high noise levels, and we returned to using only the right amplifier. We hope to resolve this problem in the future.

d. CCD hardware and software problems Several other problems surfaced during the past year of observations. Some of the images were corrupted, or had shuffled parts. The phenomenon became more frequent, leading to a loss of about 10% of the images per night. In late August 2004 we identified and replaced a faulty chip in the computer operating the camera, which had caused this problem.

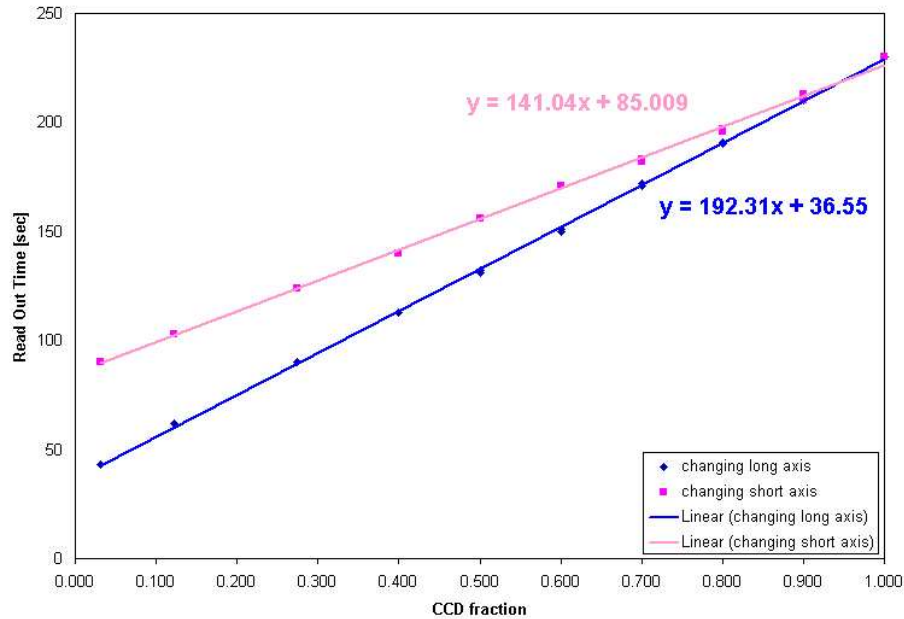


Fig. 2.5.– SITe right amplifier readout time vs. CCD size.

Another problem that arose was with the CCD overscan. The overscan is composed of several rows of pseudo-pixels, that are added to each image by reading out the chip with several more charge transfers than the number of physical columns in the chip. These pixels therefore have the bias level, and they can be used to track the bias during the night. Although the X axis overscan was set to 32 rows and was never changed by the user, the number of recorded overscan rows seemed to change spontaneously throughout the year (see Fig. 2.6). Setting the overscan manually from the program resulted in a crash. This bug was fixed by updating the software on October 20, 2004.

2.2.2 Maala Focal Reimager

a. Anti-collision measures As mentioned above, Maala can collide with the telescope pier when the telescope is pointed east of the meridian and to declinations $\delta \gtrsim 65^\circ$. A software security limit exists in the telescope setting software, preventing pointing to targets with a $\delta > 55^\circ$. However, this is not safe enough, especially since incidents

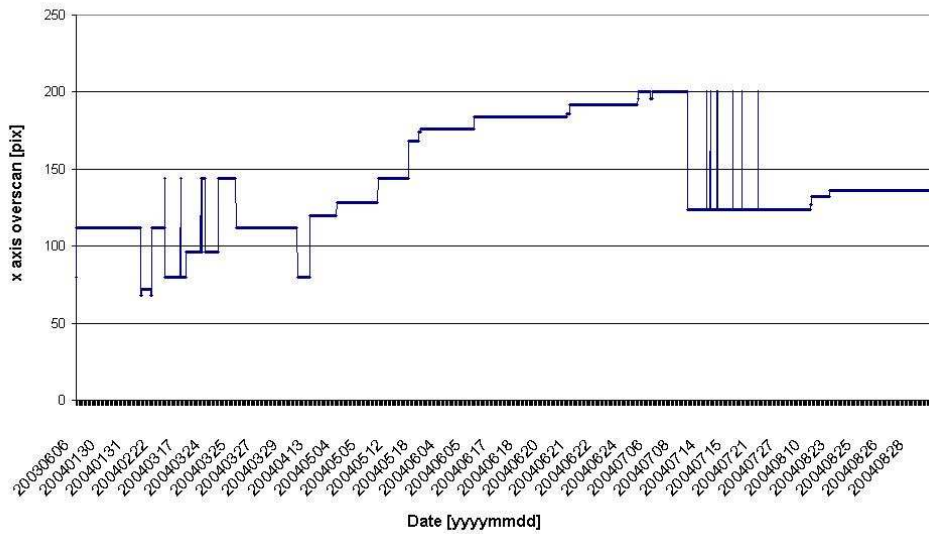


Fig. 2.6.– X axis overscan over time.

occurred when the telescope lost communication with its software, and slewed freely. Therefore, as an additional precaution, a hardware security switch was added to the telescope’s declination axis, that when closed, stops the declination motor. The system has to be reset to restart the motor. Nevertheless, the other motors that were not in use are still enabled, and since each axis (The R.A. axis and the Dec. axis) has two motors – one for fast movements (slewing) and one for small movements (setting) – the telescope can still be moved by one of the motors that has not been deactivated. This bug has yet to be fixed, so that **all** motors are stopped when the switch is triggered. Once this is fixed, remote operations from Tel-Aviv could be done.

b. Distortion fields, Maala-SITe attachment, and readout section Since the first commissioning observations with Maala, large optical distortions, due to Maala’s optical design, were evident near the edges of the large FOV (middle panel in Fig. 2.7). The distribution of the distortions over the CCD are apparently not symmetric. At first they seemed to be confined to a specific part of the CCD, rows 3000-4096 of the long axis.

We therefore decided to exclude those rows from the readout, and beginning on August 17, 2003, our read-out CCD section was changed from [1:2048,1:4096] to [1:2048,1:3000].

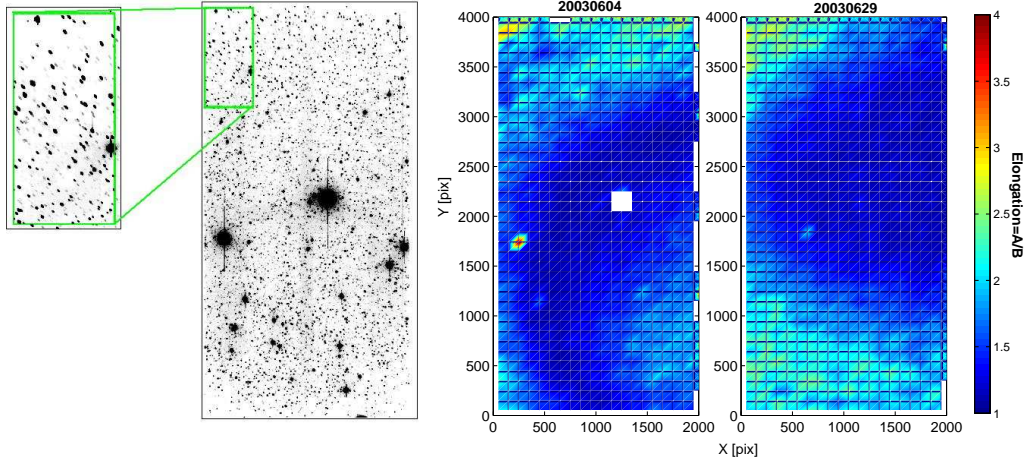


Fig. 2.7.– The distortion effect, translated to distortion maps, based on object elongation as a function of location on the CCD. *Left:* A TAVAS image of a Galactic field, used to calculate the left distortion image. The upper left corner of the image is magnified, showing distortion of stars. *Middle:* 4/6/2003 – the distortions are mostly between pixels 3000-4000 on the long axis; *Right:* 29/6/2003 – the distortion distribution has changed.

At that time, it became apparent that the distortions map changed from run to run, even though the configuration of the instruments was not altered. Two distortion maps from different runs, shown in Fig. 2.7, illustrate the changes. After some study, we concluded that the attachment of the CCD camera to Maala was not repeatable, since the fit between the connections was too tight. The Maala's base of attachment to the camera was therefore polished (October 8, 2003). By mounting the system on the telescope several times and examining the distortion maps, it was verified that the maps were now stable.

Different rotational installment positions of the SITE camera relative to Maala were tested. Distortion maps showing the elongation of objects measured across the CCD were plotted for each of the configurations (Fig. 2.8). We found the configuration with the least distortion effects, and in which the distortions are confined to a small area on the

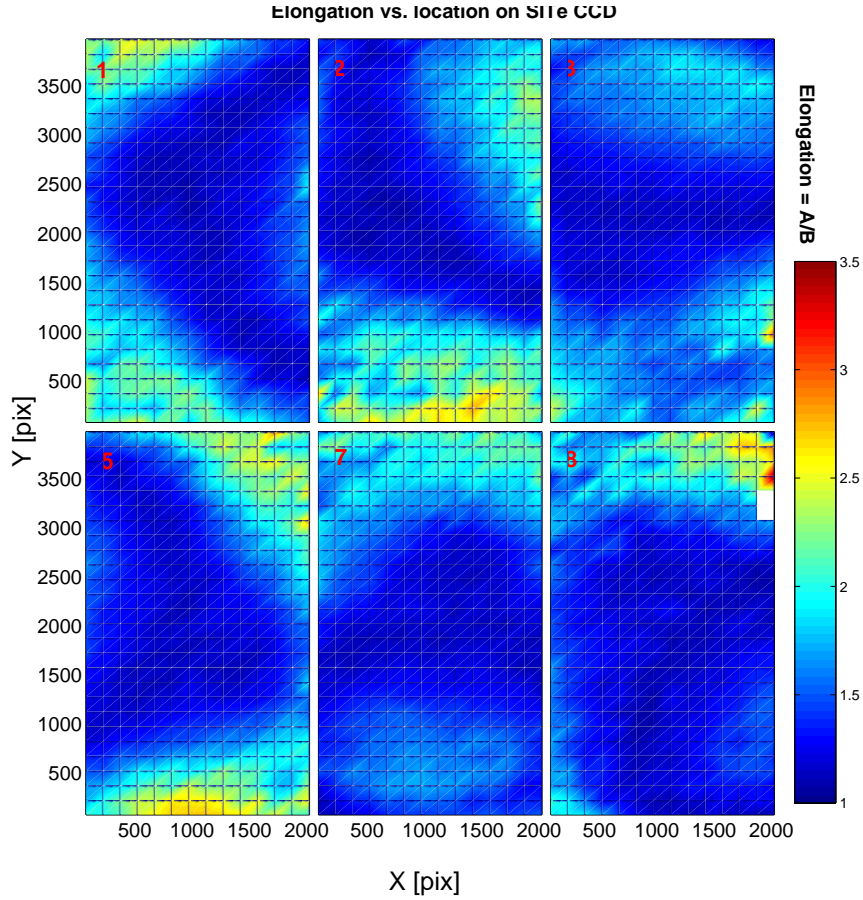
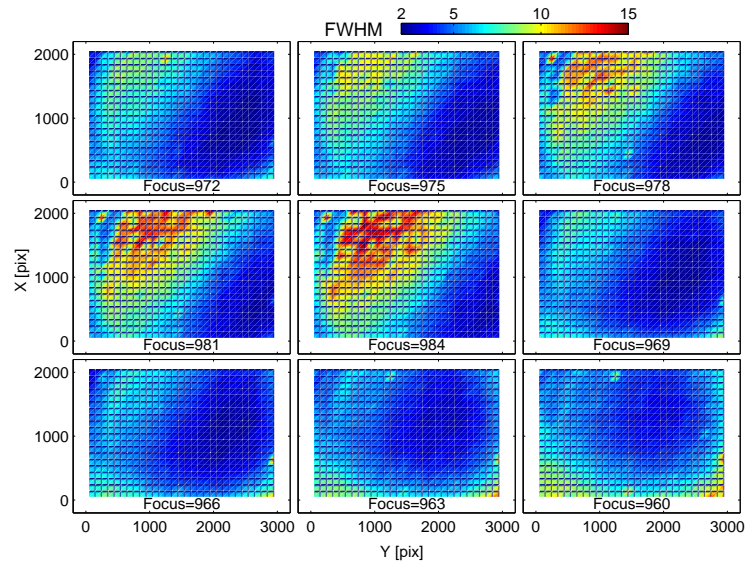


Fig. 2.8.– Distortion maps, based on object elongation as a function of location on the CCD, for eight rotational positions of the CCD to the Maala.

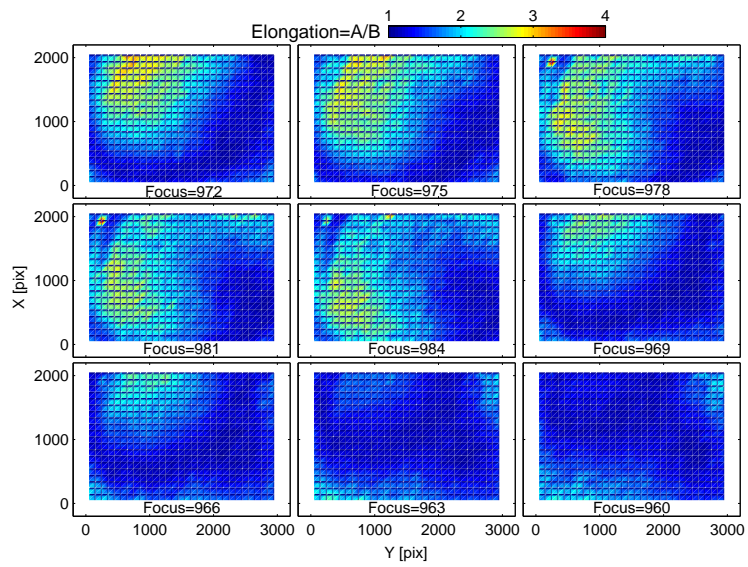
CCD (position 8 in Fig. 2.8) which could be discarded in the readout. In the chosen configuration, we read out rows 1-3000, i.e., the used area is 2048×3000 pixels, and the FOV is therefore reduced to about a 0.5 deg^2 . However, this also means we spend less time on readout, and this time is used to observe additional fields at better image quality.

c. Telescope focus The distortion distribution is unfortunately still not completely stable. One other free parameter, that affects the distortions, is the telescope focus. The focus is currently set manually, every night at the beginning of observations, by examining by eye an exposure sequence at several focus values. In a test done on the night of August

Fig. 2.9.– Distortion maps of images taken at different focus values.



(a) FWHM vs. location on CCD at different focus values



(b) Elongation vs. location on CCD at different focus values

27, 2004, nine images at different focus values (secondary mirror positions 960-984) were acquired, and for each focus position distortion maps of two kinds were plotted – the elongation as a function of location (Fig. 2.9(a)), and the full width at half max (FWHM) as a function of location (Fig. 2.9(b)). The focus the user would have picked for that night would have been 972, as it is set based on the best FWHM of objects at the image center. However, it is clear from the images that while the FWHM at the center is good, it is quite high in the upper left part of the field. Examining simultaneously the elongation, it seems that a lower focus value would be optimal. Some of this effect is due to the poor focus simply increasing the image sizes, so that their distortion is less apparent. The best way to determine the focus is to consider both effects, best FWHM and lowest image elongation (with more weight on FWHM) all over the CCD. This will be implemented in the future.

d. Current parameters TAVAS began observations starting January 29, 2004, with the following parameters: SITE position 8 (relative to Maala), Rotator angle of Maala set to 105 (so that north-south is along the short dimension of the CCD), CCD readout section is [1:2048,1:3000], gain is 5, exposure time of 210, and readout mode with two amplifiers, giving a readout time of 2 minutes (when the left amplifier is functional) or readout time of 3 minutes when using only the right amplifier.

2.3 Survey Strategy

TAVAS is planned to run for the next two years, and to receive about 70% of the telescope time, i.e., 5 nights a week. The nights will be mostly gray and dark nights, avoiding saturation on full-moon nights. 45 from the full moon, the SITE+Maala 1 pixels reach sky saturation in ~ 4 minutes. The standard exposure time of a field was set to be 2×210 sec. During dark time, the sky saturates in 30 minutes, and objects fainter than 15 mag are unsaturated. The images are unfiltered, reaching R magnitudes of ~ 21 with S/N of ~ 5 . The unfiltered imaging gives a factor of ~ 4 improvement in throughput over

standard broadbands. This allows for deep imaging with short exposures, leaving time to cover a larger survey area. During the 2-3 min readout time, the telescope can be slewed to the target. Thus an image cycle amounts to 6.5 minutes, and on an average night of 10 hours, about 85 images are obtained.

Among the 85 images, 60 images are of 30 fields that are sampled twice per night, with a time interval between re-sampling of about 15 minutes (a time interval sufficient for two other images). By comparing the two images, cosmic rays are removed (see § 3.1). Moreover, asteroids, which change position significantly over that time interval can be identified.

The fields are also generally re-observed every two weeks, allowing the detection of the sought phenomena – SNe, AGN and quasars, or any other variable phenomena with this timescale, and also providing long-term variability monitoring. Thus, after two years of the survey each field will be observed at about 20-30 useful epochs (after accounting for weather, etc.). However, there are exceptions to this sampling sequence. Some fields (extragalactic and Galactic), in which we have known objects of interest that vary on timescales of days, have a higher observing frequency, depending on the phenomenon (see the next section for more details). Also, fields with newly discovered transient phenomena, e.g., supernovae, will be observed with a higher frequency, to produce a well sampled light curve.

Another exception are some Galactic fields, in which we search for planetary transits. According to simulations by T. Mazeh and students, there is an optimal number of epochs per field, needed in order to detect efficiently a planetary transit. As can be seen in Fig. 2.10, taking into account the parameters of TAVAS, 3000 epochs per field will give the maximal number – eight – of detected transits. This will be accomplished by dedicating 25 images per night to three Galactic fields. i.e., each field will have eight exposures every night, over ~ 6 months when they are visible. Over three years, six fields will be monitored with about 3000 useful epochs.

TAVAS was therefore planned to monitor 300 fields at any given time – 30 a night \times

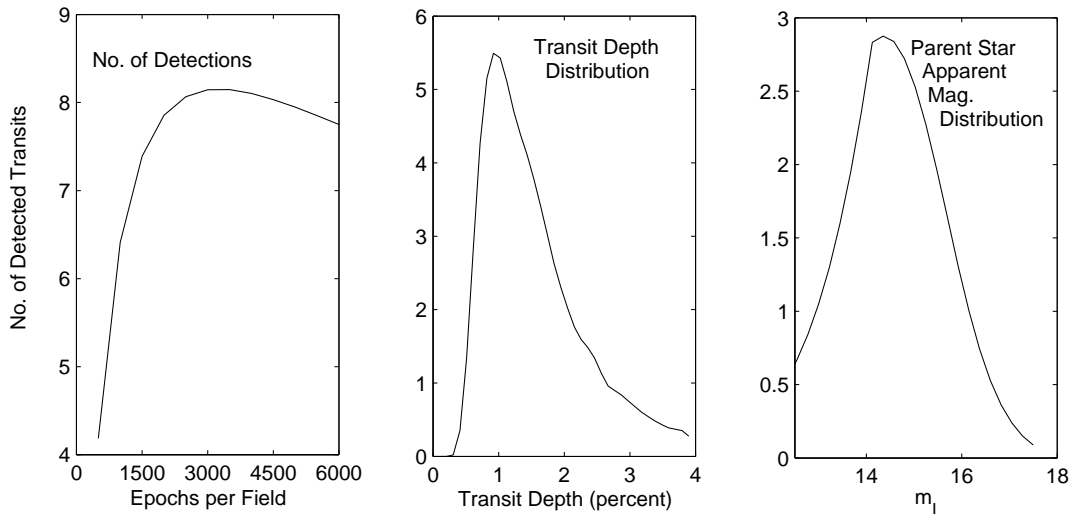


Fig. 2.10.— Simulation of expected number and properties of planet transits that will be detected with TAVAS. *Left:* Number of transits as a function of epochs per star, given a set number of pointings. *Center:* Distribution of the detected transit depths. *Right:* The magnitude distribution of the parent star in the planetary system for the detected transits.

10 nights in 2 weeks (the basic timescale unit). Since a field can only be seen for about half a year, TAVAS would have observed a total of 600 different fields, or a survey area of 300 square degrees.

The commissioning phase of the survey began in January 2004. During the first 8 months of the survey TAVAS was allocated about 25% of the telescope time. In the observing schedule for September 2004 - March 2005 TAVAS is allocated 60% of the observing time. So far we have accumulated about 100 observing nights. The current target list, of about 300 fields, produces the required relation of number of epochs per field. In the future, the target list will be enlarged.

2.4 Survey Fields

Target fields are scheduled in “quasi-transit” mode, i.e., only targets that are near the meridian at a given time are observed. This allows fields with declination of $-35^\circ <$

$\delta < +55^\circ$ to be monitored for a duration of about 6 months. Exceptions to the “transit rule” are evening and morning-twilight exposures of ecliptic fields - fields near the sun, in search of inner-Earth-orbit asteroids¹. Nightly monitoring of ongoing SNe discovered by the survey, and other events deemed necessary, will also be allowed to stretch the boundaries of the transit rule. In addition, the six Galactic fields observed for transits will be scheduled separately.

A scheduling algorithm was developed to determine the observing list for each night, which will satisfy all the requirements, and allow for follow-up of ongoing events. The algorithm ensures that every field is observed with the appropriate frequency, and transient events such as SNe have well-sampled light curves. The details of the algorithm are described in § 3.3.

The current 292 TAVAS fields are of several types, and consist of 221 “extragalactic” fields, 67 “Galactic” fields and 4 “Local Group” fields. One type of extragalactic fields are fields that have been well studied via deep, multi-wavelength imaging, or spectroscopic surveys, and for which a large body of data (e.g., object classification, photometric or spectroscopic redshifts) exists or will exist. Examples are fields in the NOAO Deep Wide Field Survey (Jannuzi & Dey 1999), the Subaru Deep Field (Kashikawa et al. 2004), the CFHT Legacy Survey (Cuillandre 2004), COMBO-17/HST-GEMS (Wolf et al. 2003), FSVS (Groot et al. 2003), the VIRMOS-VLT Deep Survey (Le Fèvre 2000), the Las Campanas IR survey (Chen et al. 2002), and selected fields covered by the SDSS (York et al. 2000). We observe a total of 48 such fields. These fields will be used to measure, among other things, field SN rates.

A second type of extragalactic fields consists of a complete subset of the ROSAT Bright Cluster Sample of galaxy clusters (Ebeling et al. 1998). Included in it are 119 X-ray-brightest clusters in the northern hemisphere, with high Galactic latitudes ($|b| \geq 20^\circ$), measured redshifts $z < 0.12$, and fluxes higher than 4.4×10^{-12} erg cm⁻² s⁻¹ in the 0.1–2.4 keV band. SNe detected in these fields will be used to measure the SN rate in

¹This asteroid search was recently concluded, and therefore ecliptic fields are no longer observed.

clusters.

A third type of fields are extragalactic and Galactic fields centered on interesting objects, whose long-term variability has been monitored at Wise over the years, or for which we have other motivation to begin monitoring now. The extragalactic fields include 54 lensed quasars, and quasar from other samples, for which we either monitor variability or aim to measure time delays.

The Galactic fields include 55 fields centered on known novae, of them six are low-Galactic-latitude fields (plus one backup field) that are sampled with high frequency to search for planetary transits, and 12 fields centered on X-ray binaries (3 HMXB; 9 LMXB) whose long-term behavior we plan to characterize.

Four more fields cover the Local Group galaxies M33 (two fields), Leo A, and Sgr Dwarf (one field each). In these fields the objective is to find distance indicators in the form of RR Lyrae stars, eclipsing binaries, and novae, as well as other transient and variable objects.

Fig. 2.11 shows the distribution on the sky of the TAVAS fields. The complete list of TAVAS fields is given in Appendix A.

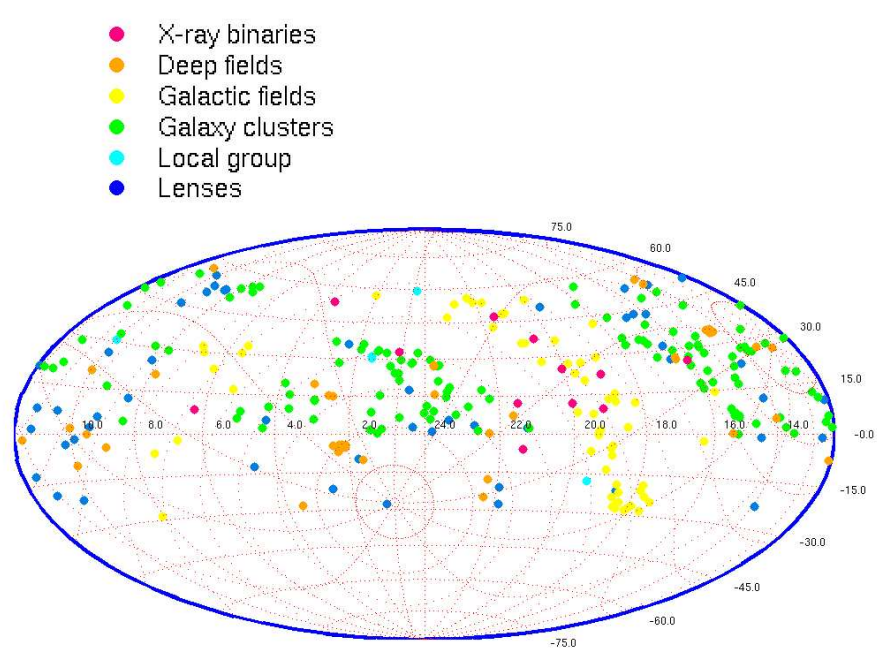


Fig. 2.11.– TAVAS field distribution in an Aitoff projection of the sky in right ascension and declination.

Chapter 3

Data Reduction, Analysis, and Archiving

TAVAS yields a large volume of data every night - nearly 1 GB of images. The survey currently uses $\sim 60\%$ of the telescope's observing time, and therefore generates about ~ 150 GB of raw images every year. From each frame, we extract between 1,000 and 20,000 sources, depending mainly on the Galactic latitude of the field. Since our goal is to find and alert on variable and transient events from these large sets of data in near real-time, there is a particular need for a fast, robust and automated data-reduction pipeline.

The TAVAS data reduction pipeline consists of several stand-alone perl modules. Each module consists of programs written in perl, C, IRAF¹, or MATLAB. The modules are grouped together by a perl shell script, where the desired modules can be chosen in advance, interactively, or operated independently, as needed. The pipeline is automatically initiated at the end of every observation night. The following sections describe the pipeline in detail. § 3.1 describes the data reduction, astrometry and photometry of the images. In § 3.2, I give a review of SQL and database systems in general, as well as a description of the SQL database we designed, and the search methods for transients and variables in the database. I describe the scheduling algorithm in § 3.3. A flowchart describing the pipeline procedures is shown in Fig. 3.1

¹IRAF is distributed by National Optical Observatories, which is operated by the Association of Universities for Research in Astronomy, Inc., under cooperative agreement with National Science Foundation.

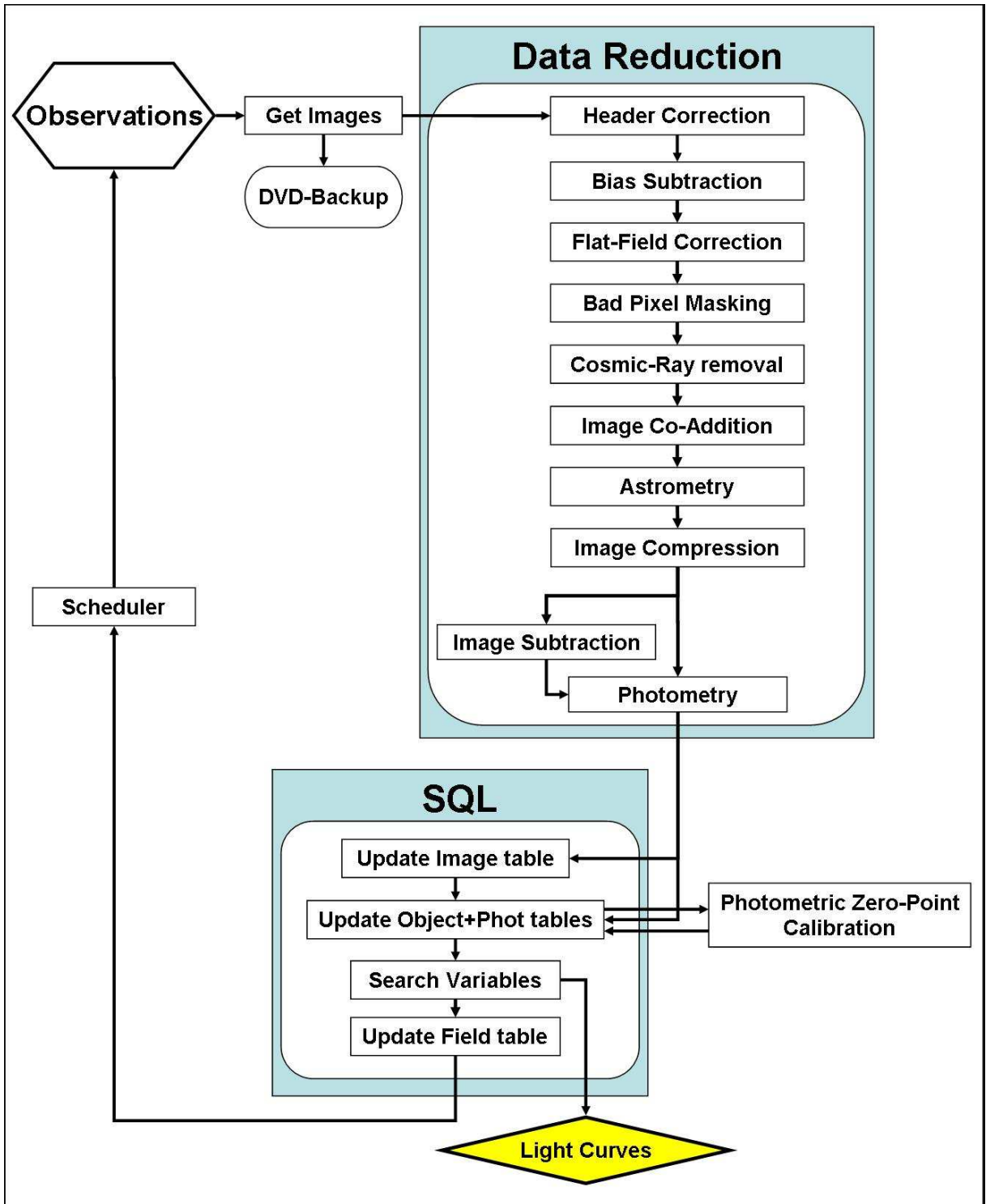


Fig. 3.1.– TAVAS pipeline flowchart

3.1 Data Reduction

The CCD data-reduction module consists of a set of IRAF routines, C programs and perl scripts. The function of the CCD data reduction module is to retrieve the images, to correct the header information, and perform bias subtraction, flat-field correction, bad-pixel correction, cosmic-ray removal, astrometry and photometry. The detailed steps are as follows:

1. Image retrieval – A typical observing night generates about 80 images, with a total data volume of 1 GB. The perl script reads the night's log file written by the camera interface, listing the images taken. The images are then automatically transferred via http protocol from the hard-disk of the data storage computer in Mitzpe-Ramon² to Tel-Aviv, where they are to be processed. The raw data are also archived on back-up DVDs.

2. Image header correction – The image headers are currently written by the SITE-CCD interface, with no input as to the telescope's actual parameters. This makes the header information inaccurate. The user can prepare a list of corrections to the header information, writing the name of a header keyword one wishes to alter, and the keyword's new value, in each line. The list is used by the script to edit the image header.

3. Bias subtraction – The bias in CCDs is a constant offset level, added to each pixel as it is being read by the on-chip amplifiers. Without this offset added, the distribution of counts would be centered near zero in an exposure with few photoelectrons, with negative and positive wings due to readout noise. However, the negative-counts information would be lost because the counts cannot be negative, and this problem is averted by the introduction of a bias level.

After careful review it is evident that the bias is not constant with time, and may change by as much as 10% from the beginning to the end of the night. To account for

²Beginning January 2005 all the data are stored also on a local computer at TAU, and so the script has been changed, to retrieve the data from the local computer directly.

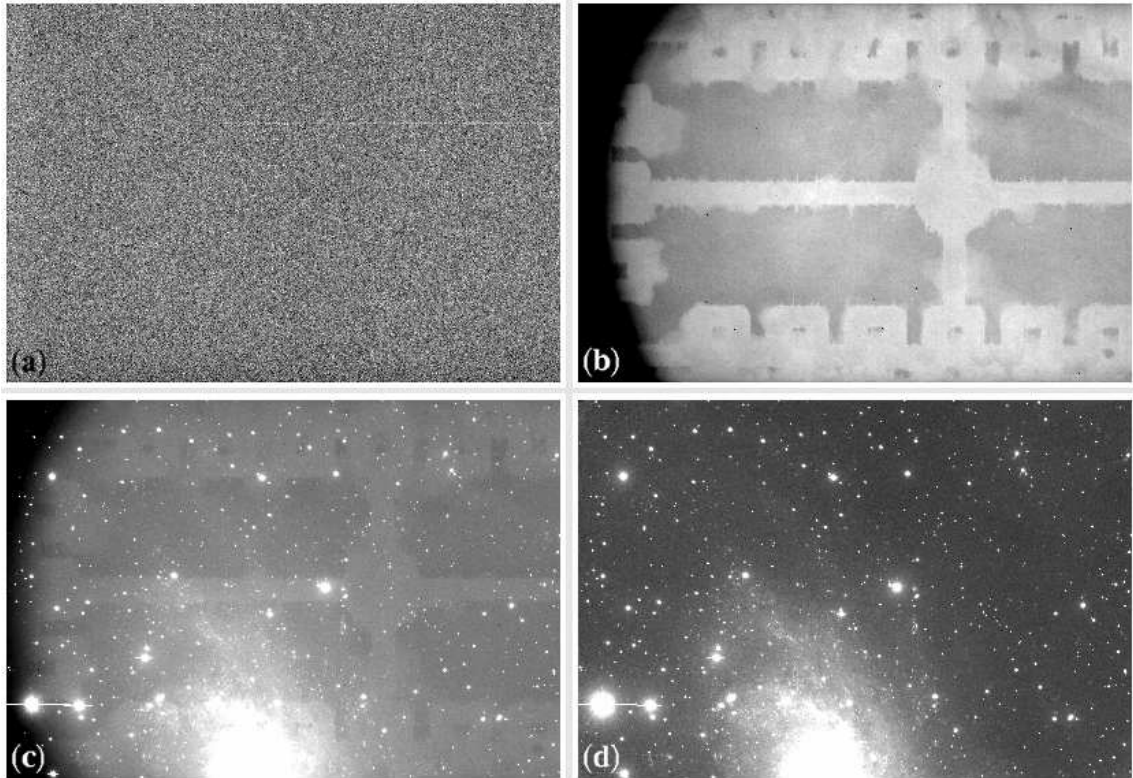


Fig. 3.2.– Sample images. (a) Bias image; (b) Super-flat-field image; (c) Raw science image of M33; (d) Image after bias subtraction & flat-field correction.

day-to-day deviations, five bias frames are taken every night, and a median bias image is created and subtracted from all the science and FF images (see Fig. 3.2(a) for an example of a bias image). An overscan region (additional pseudo-pixel columns or rows having the bias level) is added to each image to allow us to account for the intra-night changes in bias level. The overscan correction will be applied in the near future.

4. Flat-field correction – A flat-field image is a calibration image of the pixels’ relative response to radiation, due to different gain, quantum efficiency (QE), or non-uniform illumination of the CCD (“vignetting”). A flat-field can be obtained by exposing the CCD to an even illumination light source, with a high S/N. Flat correction was first attempted using dome-flats or twilight-flat images. These methods proved to be of insufficient quality in producing flat-corrected images. The reason for this is the strong

dependence of the CCD's QE on wavelength – the sky in unfiltered twilight or dome flats has a different color than the sky in science images taken during the night, and therefore different pixel responses result in poorly flattened science images if dome or twilight flats are used. The TAVAS work mode, in which many different fields are observed every night, makes it preferable and easier to use a super-flat image, that is produced every night. This is done by taking the median of all the bias-subtracted images from a given night, after running each pixel stack through a rejection algorithm. The method typically used for rejection is the “minmax” method, where the highest pixel value in every stack is rejected (other rejection options are available, see IRAF's “COMBINE” task help documentation). An example of a flat-field image is given in Fig. 3.2(b). The science images are divided by the flat-field image, which is scaled in the calculation to have a mean of 1 (the mean is written in the image header). Fig. 3.2(c) shows a science image before the bias and flat-field corrections, and Fig. 3.2(d) shows the resultant image after the correction.

Some of the fields observed are at low Galactic latitude, and their stellar density is high, making them unsuitable for composing a super-flat. In order to refrain from degrading our super-flat, images of those fields are filtered out in the combination process, based on a list of the typical stellar density for each field. If this elimination process leaves us with fewer images than needed to form a super-flat, or if not enough images were taken to begin with, a flat-field image of a previous night will be used. Another option available for the flat-field process is correction of bad-pixels in the flat-field image using a mask (see below).

5. Bad pixel masking – Bad pixels are dead or “hot” pixels, that have zero or non-linear response to light. When dividing two flat-field images that have different count levels, the bad pixels stand out in the quotient image. A list of the bad pixels is made every few months, and translated into a bad-pixel mask. The value of each bad pixel in the science image is replaced by the average of the neighboring pixel values.

6. Cosmic-ray removal – “Cosmic ray events” are produced by muon showers that form when cosmic rays hit the Earth’s atmosphere. The muons that pass through the CCD leave an ionization trail, and the liberated electrons in the affected pixel(s) are accumulated along with the photoelectrons. CR rejection is implemented using the task “CRAVERAGE” which is part of the CRUTIL package in IRAF. Cosmic rays are detected and removed using a moving block average filter algorithm: the average of the pixels inside a 5×5 box around a pixel is computed, where the central pixel is excluded. This average is used as a prediction for the value of the central pixel. If the difference between the pixel’s value and the calculated average exceeds a certain threshold (the default is ${}^{+5}_{-10}$ times the STD, calculated in a 10×10 box), the pixel is considered to be affected by a cosmic-ray. This is repeated for every pixel in the image. The algorithm can detect cosmic rays if their extent does not exceed 2-3 pixels, and it does not consider pixels within objects to be cosmic ray candidates.

7. Image co-addition – Every field is imaged several times a night. Images are aligned and combined, to give a deeper image, as follows. Objects in each image are extracted and listed using SExtractor (Source Extractor program, described below; Bertin & Arnouts 1996). The differences between their locations in the different images are used to find an initial shift of the image centers (“xyshift”, written by Eran Ofek), and a match between all the objects is found (IRAF’s “XYXYMATCH” task) using the “tolerance” algorithm (one of the optional algorithms in XYXYMATCH), that searches the sorted transformed input (based on an initial shift from xyshift) for an object closest to the reference object, within a tolerance radius. All images of a given field are aligned relative to the first image. The transformation between the matched lists is computed by IRAF’s “GEOMAP”, and is given by a fourth order polynomial. The images are translated using the polynomial fit (IRAF’s “GEOTRAN” task), where any shift, rotation or distortion between the images is taken into account. Images of poor quality (those that have a high background or were taken under poor weather conditions) are filtered out in the process; a list of typical stellar density for each field is used here as well. The aligned images are then combined using

two different methods for the following cases. When there are more than two images of a field, any residual cosmic rays are removed easily by median combination, and therefore IRAF’s COMBINE is used. In the event of only two images, we use a special algorithm (written by Assaf Horesh) to remove cosmic rays by comparing two images. It compares the same pixel in the two aligned images, and computes an STD from the surrounding pixels. If the difference between the two pixel values is higher than twice the STD, the pixel is considered a cosmic-ray, and the lower of the two pixel values is taken; otherwise, we take the average of the two pixel values. This gives a combined image which is not only deeper, but clean of cosmic rays.

8. Astrometry – The R.A.-Dec. coordinates of every source found by SExtractor are computed. Coordinates are then used for unique identification of objects that appear in different images within the database (see § 3.2). Using such a coordinate-based system enables us to easily relate our database to other databases such as the SDSS, 2MASS, and USNO. Moreover, astrometry is important in order to detect and keep track of transient phenomena. For the central part of the image, an initial shift and rotation are determined by matching the objects found near the center of the image, to sources extracted from the USNO-A2.0 catalog (Monet et al. 1998; other catalogs are optional). The image center coordinates are then used (IRAF’s “XYXYMATCH”) to find a best match between **all** objects in an image and the objects found in the catalog. A high order (second to fourth) polynomial is found (IRAF’s “CCMAP”) to describe the transformation between the objects that were matched, and the coefficients of the transformation give the astrometric solution of the image (this is similar to the procedure done in the image co-addition stage described above, only instead of a match between two images, here the match is made between an image and a catalog).

One indication for a good astrometric solution is a low STD between our solution and the catalog coordinates of the objects. Although most of our observed fields undergo the astrometry procedure successfully (about 90% of the fields), the STD of the solution is still high compared to other surveys. Residuals are large (a few arcsecs) in some parts

of the image, where there are distortion effects due to the Maala optics. Currently, the typical STD is 0.6 arcsec in R.A., and 0.4 arcsec in Dec.. In some Galactic fields with high stellar density, our astrometry fails altogether, i.e., the STD is higher than 1.0 arcsec, which we have set as the acceptable upper limit. One other parameter to examine is the number of objects used in the matching process. An astrometric solution found based on just a few objects may not be a real solution. This may happen if the field is too crowded, or if the coordinates of the center of the image given in the header are incorrect. The lower limit we set for this parameter is 10 objects. If an astrometric solution is not found, the image is not written to the output list, and is not further analyzed.

9. Image compression – The images pixel values are converted from real to integer format. This is done in order to save disk space, as real images occupy twice as much disk space as integer images. To limit the loss of information due to digit rounding, the pixel values are first multiplied by a constant (2.9), to increase the dynamical range from 1 to 22,598 (the estimated saturation level) to the range of 1 to 65,534. Subsequently, the original gain (5) is divided by the same constant, to give the gain of the compressed images (1.724).

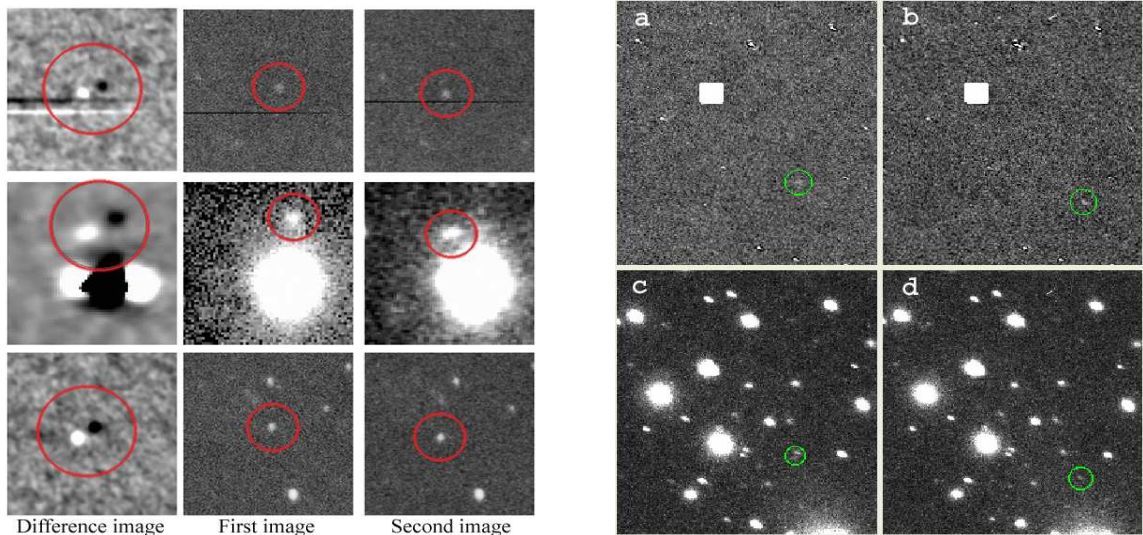
10. Photometry – The SExtractor program is used to perform aperture photometry on all the images. SExtractor was found to be the best choice for a photometry program. Its inputs are easy to change and control, and it has many optional catalog output parameters. It is fully automated and works from a command line, making it easy to incorporate into our pipeline. Also important, SExtractor has the ability to work on relatively large images. We compared by eye its detection efficiency to other programs – IRAF’s “DAOFIND”, and NANFSTAR (written by N. Almoznino). SExtractor detects more real objects, while ignoring cosmic rays that are spread over a few pixels. All the programs had problems identifying extended objects (objects with high ellipticity due to distortions at the edges of the field), where single objects were broken into two. However, SExtractor showed better overall performance in this area as well. All programs have difficulty in deblending

objects near bright stars, but this is still best accomplished with SExtractor, and along with the saturation flag it produces, those objects can be marked and dealt with later. In terms of speed, SExtractor works significantly faster than the other two programs tested. To summarize, the SExtractor program gave answers to many problems specific to the TAVAS fields, which were unsolved by the other programs, and had better results in comparison.

SExtractor gives the following flags to each object it identifies: saturation, deblending of the object from neighboring objects, and bad pixels within the object, according to the mask image. The magnitudes of sources are measured inside three fixed apertures - 4, 6 and 8 pixels in diameter. We also measure two other magnitudes, labeled AUTO and ISO, and their errors. The ISO method gives the isophotal magnitude derived from the counts above the detection threshold, minus the background. The AUTO method calculates an elliptical aperture according to the object's light distribution (this is inspired by Kron's "first moment" algorithm; Kron 1980), and gives the magnitude within that aperture. The AUTO method is said in the SExtractor manual to give the most precise estimate of total magnitude, at least for galaxies, which are extended objects. AUTO will avoid flux loss both in galaxies and in other extended sources, such as distorted objects. In some fields, such as galaxy clusters, the AUTO estimate is optimal, whereas in Galactic fields, which are crowded with sources, a fixed aperture is preferable. However, the main reason for measuring magnitudes with all these different methods and apertures is the variation in the point-spread-function (PSF) of objects over the field of view. This problem can be monitored by examining the relations between magnitudes of different apertures, as a function of location on the CCD, and can improve our derivation of the photometric zero-point of every image. Finally, having several options will help determine, over time, which method is the best method for TAVAS photometry - fixed aperture, AUTO, or isophotal.

11. Image subtraction – Another method we intend to explore for finding variability is PSF matching and image subtraction. Image subtraction is the optimal method to

Fig. 3.3.– Image subtraction examples



(a) Difference image (*left*) for two epochs (*center* and *right*) showing three cases of asteroids found, using the CPM method.

(b) Difference images (*a, b*) of two epochs (*c, d*), in which each epoch was subtracted from a deep reference image, using the “optimal PSF matching” algorithm. Circled is an asteroid appearing in the two images, taken about 20 minutes apart.

detect and measure variable point sources in crowded fields (e.g., our Galactic fields) or on top of bright backgrounds (e.g., galaxies in our SN search).

Two algorithms for image subtraction were tested on TAVAS images. The first is the “optimal PSF matching” algorithm, which is based on Alard & Lupton (1998) and Alard (2000). With this method, which works best in crowded fields, a minimized convolution kernel transforming from the reference to the sample image is computed in small areas of the images, based on the PSFs of the two images. The calculations are done in real space, rather than Fourier space. The second method tested, the “Common PSF Method” (CPM, aka “Double Degradation Algorithm”, DDA, Gal-Yam et al. 2004) convolves the PSF measured in the image with the PSF measured in the reference image, and vice versa, and then subtracts the convolved images.

We have carried out only some preliminary attempts at image subtraction in TAVAS. Some examples can be seen in Fig. 3.3(a), where the CPM method was used, and in Fig. 3.3(b), where the “optimal PSF matching” algorithm was used. As apparent, specifically in the latter, some residuals are left, due to significant variations of the PSF between the different images. Further investigation will be done in order to improve and adapt image subtraction to our survey.

3.2 The SQL database

The main goal of TAVAS is to monitor millions of objects, and to enable efficient searches for particular types of variable and transient behavior. Such an ambitious project calls for efficient data storage and management, where required information can be both saved and accessed easily and quickly. As with many other large surveys, this need was met by developing a relational database (DB) using SQL – “Standard Query Language”.

A database is a collection of data organized so that it can be easily accessed, managed, and updated. In a **relational** database, the information is stored in tables that can relate to each other by a common field. If a datum is changed in one table, it will be changed in all related tables. Tables contain data fitted into predefined categories. A table consists of one or more columns, and of rows (see example of a table below). Each column stands for a different category. Each row holds a unique data record.

The best logic to follow in designing a database is to store the data efficiently, i.e., with as few repeated fields as possible. This is done by constructing a few smaller tables of different topics, each storing different information, and conceptually-connecting them with “keys”, rather than storing everything in one large table. For example, instead of saving the information on the images taken in the survey in the following way:

ImageTable			
<i>ImageName</i>	<i>JD</i>	<i>FieldName</i>	<i>Field_ra_dec</i>
20041102.034	2453312.34	J0011+3225C	(2.946,32.42)
20041102.037	2453312.36	J0011+3225C	(2.946,32.42)
20040604.063	2453161.53	J0018+0256L	(4.547375,2.94)
20040604.066	2453161.55	J0018+0256L	(4.547375,2.94)
20040604.069	2453161.56	J0018+0256L	(4.547375,2.94)

we will divide the information into two tables - an Image table, and a Field table:

ImageTable			FieldTable		
<i>ImageName</i>	<i>JD</i>	FieldID	FieldID	<i>FieldName</i>	<i>Field_ra_dec</i>
20041102.034	2453312.34	1	1	J0011+3225C	(2.946,32.42)
20041102.037	2453312.36	1	2	J0018+0256L	(4.547375,2.94)
20040604.063	2453161.53	2			
20040604.066	2453161.55	2			
20040604.069	2453161.56	2			

This way, there is no redundancy in the Image table. Only one column – FieldID, references the Image to its appropriate Field information (field name, R.A-Dec., etc). The relation between the two FieldID columns is termed “one-to-many” - one entry of FieldID in the Field table corresponds to many entries of FieldID in the Image table. In the DB terminology this is referred to as **normalization** (see Codd 1970 for database normalization rules).

Keys, which are indices in the mathematical sense, are used to relate, sort, and speed up the access to the tables. A key will be defined on a field that is used frequently in operations. A primary key is defined on one or more columns whose values uniquely identify each row in a table. A foreign key is used to relate two columns that represent the same category in different tables. In the example above, the foreign key is defined on the FieldID column of the Image table, linked to the FieldID column of the Field table, which must be a primary key of that table. It allows cascading-deletes and -updates, i.e., if a record has been deleted in the primary table (Field table), the delete “cascades” through the subordinate tables (Image table).

SQL is a standard computer language developed for accessing and manipulating relational database management systems (RDBMS). It is used to communicate with the

database. SQL is the most widely used language to manage RDBMS. It enables fast extraction and data updates. It stores the data compactly and efficiently, thus saving storage space and computational power. The syntax is very simple, making it easy to learn, work with and program. The DB tables are created once using the “CREATE TABLE” syntax. The main SQL statements used to manage entries in the DB tables are: “INSERT”, “UPDATE” or “DELETE”. An SQL query is a question performed on the DB tables, allowing for data to be extracted in a flexible way and resulting in a table. For this the “SELECT” statement is used. For example, such a query would look like:

```
“SELECT ImageID,ImageName FROM ImageTable WHERE airmass>2.0;”.
```

Here, “ImageID,ImageName” are the columns to retrieve, which are part of “ImageTable”, and the “WHERE” clause specifies the condition - we want images that were taken at air-mass higher than 2.0. Note that the airmass information is also stored in the ImageTable, as another column, even though not specified explicitly in the columns to retrieve.

The SQL version we use to build and manage the TAVAS database is called PostgreSQL (Stonebraker & Rowe 1986; see <http://www.postgresql.org>). It is compatible with SQL syntax, and includes additional useful features: issuing complex queries and sub-queries, extending the language by adding data types, functions and operators, and a simple backup and recovery tools. Another important feature is the option of geometric data types, (e.g., point, circle, etc.) which is advantageous for describing two dimensional space, as relevant for the case in astronomy.

3.2.1 Design of the TAVAS database

The TAVAS database consists of four major tables – a *Field* table, an *Image* table, an *Object* table and a *Phot* table. The relations between the tables are illustrated in the hierarchy diagram (Fig. 3.4). The full column information for each table is detailed in Appendix B.

The *Field* table consists of all observed fields, which are reviewed in § 2.4 (see a full list in Appendix A). Each entry describes the essential properties of a field – its name,

coordinates, the frequency with which we want to observe it, limiting hour angle (H.A.) for observation, and some additional information required to schedule future observations. Each field is identified by an incremental *FieldID* assigned to it, defined as primary key (PK) of the table. This table hold some 300 entries, and may grow, as the field list will be extended to fit the growing telescope time allocation. Also, when a non-TAVAS field (e.g., occasional observations for the other programs) is observed, it is added to the table with a “non-TAVAS” flag.

The *Image* table holds a list of all the images that have been taken in the survey. Each entry is an image, uniquely identified by a PK called *ImageID*. The other columns hold various information related to the image. Most of these details are extracted from the image-header that was recorded when the image was taken, such as R.A.-Dec, airmass, H.A.. Some header keywords were written by the astrometry process – the plate solution and STD, and others were added by the photometry process – limiting magnitude, mean elongation of objects in the image, zero point and seeing. Because many images record the same field, one column in this table is the *FieldID*, connected to the *Field* table’s *FieldID* column, and thus to the data stored in that table. This relation is constrained with a foreign key, where the type of the relation is one-to-many. The *Image* table is updated daily with the new images, approximately ~ 100 new entries every night.

The *Object* table lists all the objects observed in the survey, i.e., each entry is a unique source that appears in one or more images. This table holds a PK called *ObjectID* for each object, its mean R.A.-Dec, mean magnitude (both calculated from all of its occurrences), proper motion, object class, and some other properties. Since many objects belong to the same field, a *FieldID* column connects each entry to the *Field* table, in the same manner that the *Image* table was connected to the *Field* table. A field has typically about 5000 objects, and there are 300 survey fields. After a year into the survey, the *Object* table ought to have about a million unique objects, and should not grow considerably bigger, once all the fields have been observed at least once.

The last main table is the *Phot* table. The *Phot* table consists of the astrometry and

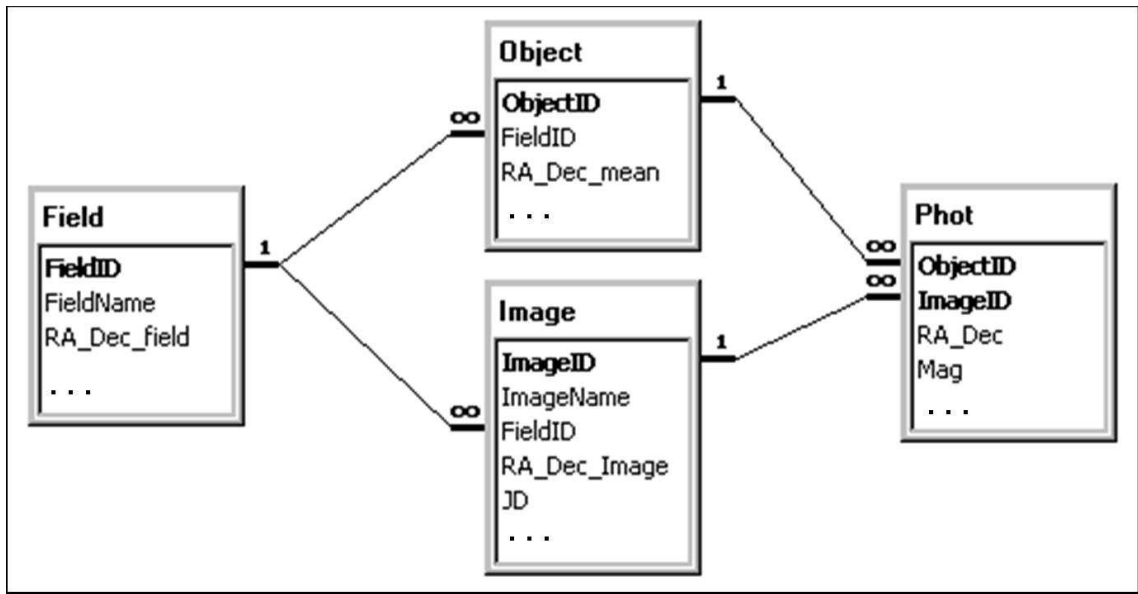


Fig. 3.4.– TAVAS database hierarchy diagram. The bold-faced columns serve as the primary key of that table. Lines show the one-to-many ($1 \rightarrow \infty$) relations between tables.

photometry data for all the occurrences of the objects in all the images. The *Phot* table is essentially a product of the *Image* table and the *Object* table - each image has many entries in this table, as many as the number of objects identified in the image, and each object appears many times in the table, as many as the number of times the object was identified in different images. The table therefore has a PK that is uniquely defined by the combination of two columns: one is *ImageID*, connected to the *ImageID* column in the *image* table; the other is *ObjectID*, connected to the *ObjectID* column of the *Object* table.

Every night some 5000 objects are identified in each image, and about 100 images are generated. This corresponds to $\sim 500,000$ new entries to the *Phot* table, every day. This constitutes the largest, most important table in the DB. It is expected to add up to about 50 million entries after the first year. This is why it is important to design this table as efficiently as possible - with the necessary columns only, and to choose their data types to be the most compact. The columns in this table are: location (RA-Dec,

X-Y), the five types of magnitude and their errors, and the SExtractor flags provided by the photometry. The *Phot* and the *Object* tables are being populated simultaneously by the same module. The module is a perl script, that has a special database interface (DBI) that communicates with the PostgreSQL server. It first makes a list of all objects belonging to the field, for a given image, and matches it to the photometry file of the image. The match is done using IRAF's "XYXYMATCH". Matched pairs are inserted to the *Phot* table, and the parent object in the *Object* table is updated accordingly. Those that were not matched, are added as a new object to the *Object* table, and an entry is made to the *Phot* table with the new corresponding *ObjectID*.

3.2.2 Searching the database

An algorithm for finding transient and variable phenomena is under construction. The main idea is to query the *Phot* table for *ObjectIDs* whose magnitude has changed by more than a certain level and then disqualify those that fall in the noise section - cosmic rays, bad pixels, other defects in the image, limiting magnitude effects or field edge effects.

3.3 The Scheduling Algorithm

As a last stage of the pipeline, the database is used to prepare an observing schedule for the following night of observation. In order to follow the fields in quasi-transit mode, observe each field with its characteristic sampling rate, and follow the strategy outlined in § 2.3, the following rules and limitation are implemented in the scheduling algorithm we have designed, determining which fields are to be scheduled in a given time interval:

1. Fields with airmass < 2.5 . This limit is a parameter and can generally be changed for each field, but at this value it ensures that no aberrations will be introduced due to high airmass.
2. Fields with Hour-Angle (HA) < 1 hour. This limit implements the quasi-transit mode.

3. Fields that are not affected by the Moon’s brightness by more than 3 magnitudes. This is calculated according to a model presented by Krisciunas & Schaefer (1991):

$$I^* = 10^{-0.4(3.84+0.026|\alpha|+10^{-9}\alpha^4)}, \quad (3.1)$$

$$f(\rho) = 10^{5.36}[1.06 + \cos(\rho)^2] + 10^{6.15-\rho/40}, \quad (3.2)$$

$$X(Z) = (1 - 0.96 \sin^2(Z))^{-0.5}, \quad \text{and} \quad (3.3)$$

$$B_{moon} = f(\rho)I^*10^{-0.4k_{ext}X(Z_m)}[1 - 10^{-0.4k_{ext}X(Z)}]. \quad (3.4)$$

where I^* is the illuminance of the moon outside the atmosphere, α is the lunar phase angle, ρ is the angular separation between the object and the moon, $f(\rho)$ is the scattering function in the atmosphere, $X(Z)$ is the airmass calculated for object zenith distance Z , and for Z_m , the zenith distance of the moon. B_{moon} is then calculated for k_{ext} , the extinction coefficient, which we take to be 0.3 mag/airmass. From it, the change in the V-band sky brightness caused by the moonlight is then:

$$\Delta V = -2.5 \log[(B_{moon} + B_{Sky})/B_{Sky}] \quad (3.5)$$

where we take the dark sky surface brightness to be $B_{Sky} = 21.7$ mag/arcsec².

4. Each field should be observed twice during the night.
5. Fields of different types should be observed with different frequency, i.e., extra-Galactic fields, where SNe are expected to be found, should be revisited every two weeks; fields of CVs or other short-period phenomena, should be revisited every day, etc. Follow-up fields are also given high frequency, to get a better sampling. This is set by a time interval parameter that is assigned to each field. From the required frequency, a “weight” is found for each field, using a Fermi-Dirac-like function. It is calculated around the time elapsed since a field’s last observation, minus its time interval (in days):

$$Weight = 1 - \frac{1}{\exp\left(\frac{(JD_{Start} - JD_{Last}) - TI}{TI_{Err}}\right) + 1}, \quad (3.6)$$

where JD_{Start} is the time at the beginning of the interval, JD_{Last} is the time of the field's last observation, TI is the (sampling frequency)⁻¹ and TI_{Err} is the width of the step of the function. A weight close to 1 is given to a field that has not been observed for a long time, and close to 0 to one that has been observed recently.

The scheduler extracts the above parameters (airmass limit, H.A. limit, time interval and time interval error) using a simple SQL query on the Field table (see § 3.2.1), where the parameters are stored and can also be altered individually for each field. The algorithm then computes the airmass, H.A., moon brightness, and weight for each field, starting with the beginning of the night. After it filters out the fields that violate rules 1-3, the algorithm selects three fields with the highest weight. The three-field group is repeated, to satisfy rule 4.

The time variable (JD_{start}) is advanced by the accumulated exposure time, and the process continues iterating until it reaches the end of the night.

Chapter 4

Current Status and Future Tasks

In this thesis I have described the planning, commissioning and initial implementation of TAVAS. To summarize, TAVAS is an optical variability survey, conducted with the Wise 1-m telescope in Mitzpe-Ramon, aimed at the discovery of various new variable and transient objects, and the monitoring of known phenomena. A detailed observational plan has been outlined, in which 150 deg^2 of the sky are observed regularly, with timescales from hours, to months and years. Achieving real-time automated analysis of large amounts of data is a critical task, in order to guarantee identification and follow-up of new discoveries. For this purpose a data reduction and analysis pipeline has been designed and developed, where the images are processed, analyzed, and the extracted object information is archived on a nightly basis.

TAVAS has been operational for almost a year, and first results are now beginning to emerge. Searching the database has not yet been initialized, but some conclusions have become clear from the data accumulated. In this chapter I will show a few examples of variable objects found with TAVAS, outline the present status of the project, and discuss future work.

Basic reduction and inclusion of the data in the database is working in a fully automated mode, every morning following observation. We have accumulated over 100 nights of observation, and are currently working on calibrating the photometry in order to bring all the images to the same photometric zero-point.

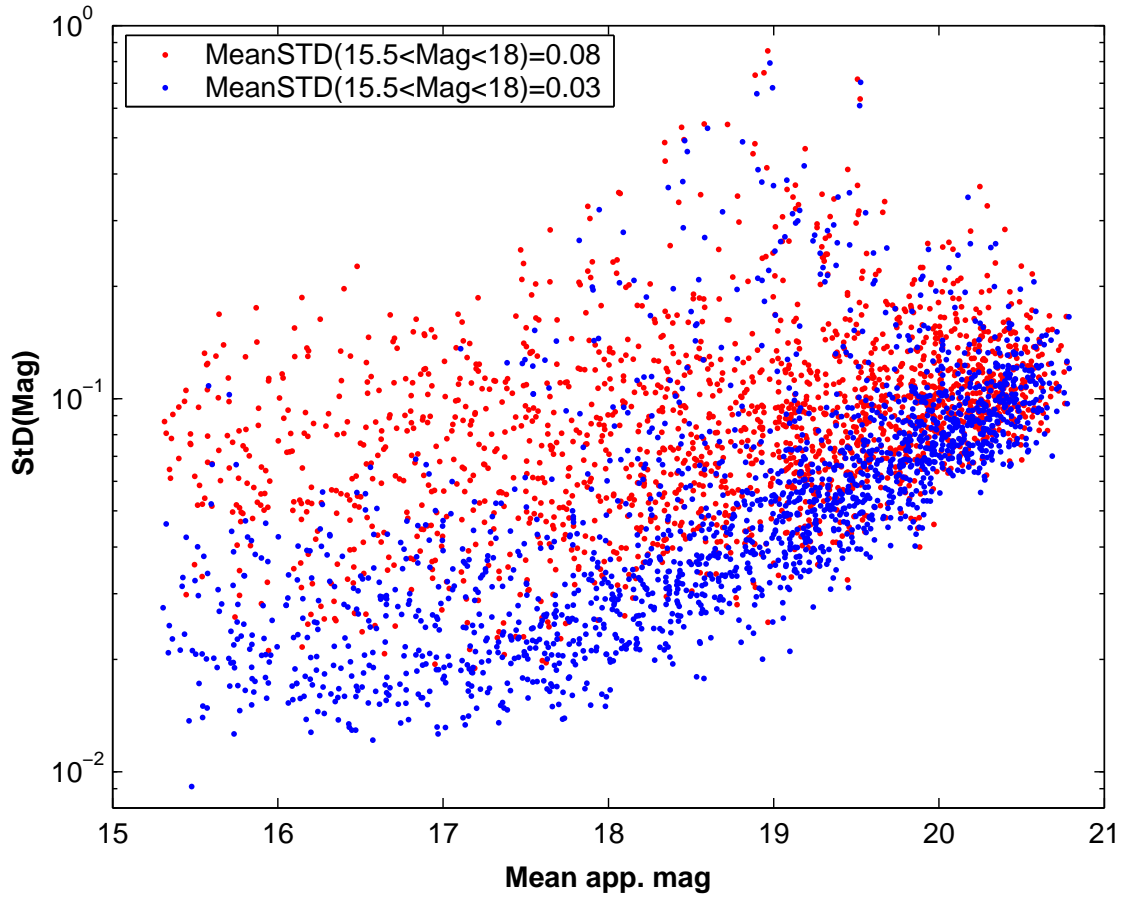


Fig. 4.1.– Photometric accuracy of TAVAS, shown as $\text{STD}(\text{mag})$ vs. mean apparent mag, based on ~ 2000 objects (appearing in more than 60% of the images) in the galaxy cluster field J0459+0846C, observed on 15 good epochs out of 20. The red dots show the scatter with no correction. For the blue dots, a positional correction is included, as described in the text.

After the first few attempts of relative photometric calibration of some fields, it is apparent that there exists some confusion in the unique identification of objects. The R.A.-Dec registration we have adopted is probably introducing large uncertainties, causing this confusion. Consequently, we are now trying a different method of registration whereby only the reference image undergoes astrometry, and all other images of that field are aligned with it. The object information would then be saved according to pixel, rather than celestial, coordinates. Nonetheless, the celestial coordinates will be attainable

through the reference image coordinates. A preliminary relative photometric calibration using the aligned images has been developed, where a relative zero-point correction is calculated for each image. A weighted average is taken over the magnitude differences between each object in the image and its counterpart in the reference image. As a first order correction, the magnitude difference is also characterized as a function of position in the image. This is done by fitting a two-dimensional polynomial for a zero-point correction as a function of position in the image, thus correcting for image distortion effects. An example is shown in Fig. 4.1. The standard deviation from the mean magnitude for each object is plotted as a function of magnitude, where the red dots show the results with no correction, and the blue dots include the positional correction. Taking into account the positional correction reduces the mean photometric error from 8% to 3%, for stars in the magnitude range 15.5 to 18. At fainter magnitudes, the error increases as expected from Poisson statistics.

In order to obtain some preliminary results, we have used these calibrated data to hand-pick some variable objects. For each object chosen from Fig. 4.1, a calibrated light curve has been plotted, and a power spectrum was calculated and plotted. The highest peaks in the power spectrum correspond to the most probable frequencies in the dataset. The light curves in Fig. 4.2 are folded over the period deduced from the high peak in the power spectrum for objects with $\text{power} \gtrsim 10$. These are examples of variable objects.

The principal tasks remaining in the near future are the following. More work needs to be done to improve the photometric accuracy. We intend to try a higher order polynomial fit to the zero-point as function of image location. Once we obtain satisfactory results, we will integrate the algorithm into the database.

The database infrastructure has been implemented, and its loading tools are ready. However, daily routines need to be designed to maintain and administer the database. Currently, the largest table (*Phot*) size is about 3.5 GB, containing 25 million entries so far. It is now at a point where it is considered large by database standards, and although typical queries still take a matter of seconds, its performance needs to be tweaked. To this

end, we intend to consult with outside database experts, as our experience in the matter is limited. As a final step, search and alert routines will be designed to communicate with the database.

Image subtraction, as mentioned above, is also planned. It is important to follow this path, as it will reveal variable and transient objects that are not detectable with simple aperture photometry.

More fields need to be added to the field list, as the project is now allocated more telescope time. Routine remote operation of the telescope from Tel-Aviv is planned once the mechanical safety trigger on the telescope is adjusted so that when activated, all telescope motors stop. The software at the observatory that controls the CCD camera is not incorporated into the remote observation software, which operates and monitors all the other components at the observatory. Once this is done, better control of all the equipment will be achieved, and this will also solve the header information problem, as the positional information will come directly from the telescope, rather than from a prepared list.

Finally, and in parallel to these remaining technical tasks, the scientific yields of TAVAS can start to be mined, both in the field of real-time and follow-up of transient phenomena, and in the area measurement and characterization of the variability data accumulating in the database.

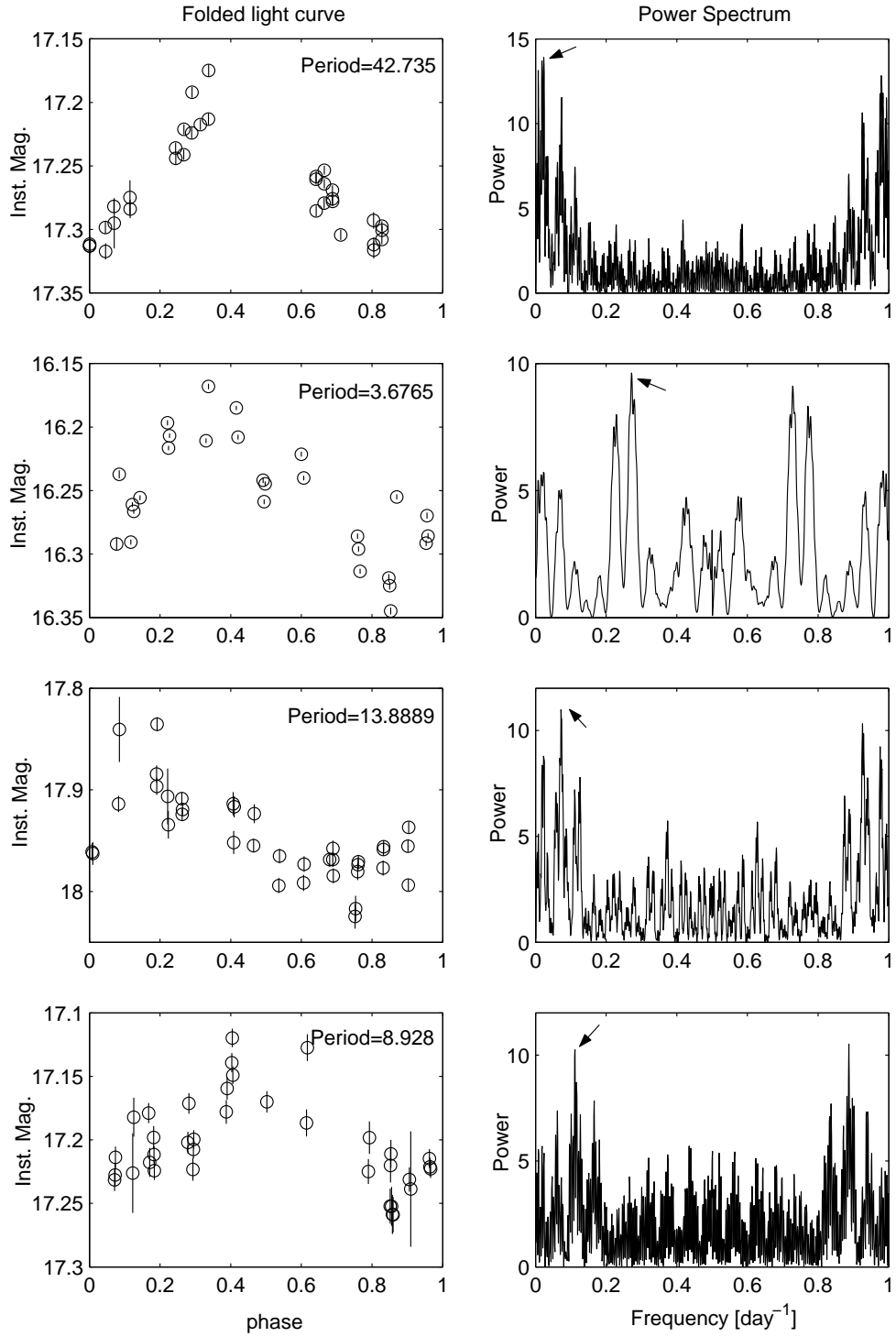


Fig. 4.2.– Examples of variable objects. *Left:* Light curves of four objects in Field J0459+0846C, folded over the period. *Right:* Power spectrum, for each of the corresponding light curves. The period is deduced from the frequency of the highest peak, where variability is found for peaks higher than $\gtrsim 10$ (pointed by arrows).

Bibliography

Afonso, C., et al. 2003, , 400, 951

Alard, C., & Lupton, R. H. 1998, , 503, 325

Alard, C. 2000, , 144, 363

Alcock, C., et al. 2000, , 542, 281

Alcock, C., et al. 2001, , 321, 678

Andersen, J. 1991, , 3, 91

Ansari, R., et al. 1997, , 324, 843

Ansari, R. 2004, astro-ph/0407583

Ansari, R., et al. 2004, , 421, 509

Aubourg, E., et al. 1993, , 365, 623

Becker, A. C., et al. 2004a, astro-ph/0409167, To appear in Proceedings of IAU Symposium 225: Impact of Gravitational Lensing on Cosmology

Becker, A. C., et al. 2004b, , 611, 418

Belokurov, V., et al. 2005, , 357, 17

Bertin, E., & Arnouts, S. 1996, , 117, 393

- Bopp, B. W. 1974, , 193, 389
- Bouchy, F., Pont, F., Santos, N. C., Melo, C., Mayor, M., Queloz, D., & Udry, S. 2004, , 421, L13
- Brown, T. M., Charbonneau, D., Gilliland, R. L., Noyes, R. W., & Burrows, A. 2001, , 552, 699
- Charbonneau, D., Brown, T. M., Latham, D. W., & Mayor, M. 2000, , 529, L45
- Charbonneau, D., Brown, T. M., Noyes, R. W., & Gilliland, R. L. 2002, , 568, 377
- Charles, P. A., Coe, M. J., 2003, astro-ph/0308020, To appear in "Compact Stellar X-ray Sources", eds. W.H.G. Lewin and M. van der Klis
- Chen, H., et al. 2002, , 570, 54
- Codd, E. F. 1970, "A relational model of data for large shared data banks", Communications of the ACM 13, 377–87.
- Croom, S. M., Smith, R. J., Boyle, B. J., Shanks, T., Miller, L., Outram, P. J., & Loring, N. S. 2004, , 349, 1397
- Cuillandre, J. 2004, SF2A-2004: Semaine de l'Astrophysique Francaise, meeting held in Paris, France, June 14-18, 2004, Eds.: F. Combes, D. Barret, T. Contini, F. Meynadier and L. Pagani EdP-Sciences, Conference Series, meeting abstract
- de Jong, J. T. A., et al. 2004, , 417, 461
- Delfosse, X., Forveille, T., Mayor, M., Burnet, M., & Perrier, C. 1999, , 341, L63
- Ebeling, H., Edge, A. C., Bohringer, H., Allen, S. W., Crawford, C. S., Fabian, A. C., Voges, W., & Huchra, J. P. 1998, , 301, 881
- Gal-Yam, A., Maoz, D., & Sharon, K. 2002, , 332, 37

- Gal-Yam, A., Maoz, D., Guhathakurta, P., & Filippenko, A. V. 2003, , 125, 1087
- Gal-Yam, A., et al. 2004, , 609, L59
- Gehrels, N., et al. 2004, , 611, 1005
- Giveon, U., Maoz, D., Kaspi, S., Netzer, H., & Smith, P. S. 1999, , 306, 637
- Graham, M. J., et al. 2004, *Astronomical Society of the Pacific Conference Series*, 314, 14
- Groot, P. J., et al. 2003, , 339, 427
- Harmon, B. A., et al. 2004, , 154, 585
- Hartwick, F. D. A., & Schade, D. 1990, , 28, 437
- Henry, G. W., Marcy, G. W., Butler, R. P., & Vogt, S. S. 2000, , 529, L41
- Horne, K. 2003, *Astronomical Society of the Pacific Conference Series*, 294, 361
- Jannuzi, B. T., & Dey, A. 1999, *Astronomical Society of the Pacific Conference Series*, 191, 111
- Kaiser, N., & Pan-STARRS Project Team 2004, *American Astronomical Society Meeting Abstracts*, 204
- Kaluzny, J., Kubiak, M., Szymanski, M., Udalski, A., Krzeminski, W., & Mateo, M. 1996, , 120, 139
- Kashikawa, N., et al. 2004, , 56, 1011
- Kaspi, S., Smith, P. S., Netzer, H., Maoz, D., Jannuzi, B. T., & Giveon, U. 2000, , 533, 631
- Kochanek, C.S., Schneider, P., Wambsganss, J., 2004, Part 2 of *Gravitational Lensing: Strong, Weak & Micro*, *Proceedings of the 33rd Saas-Fee Advanced Course*, G. Meylan, P. Jetzer & P. North, eds. (Springer-Verlag: Berlin)

Konacki, M., Torres, G., Jha, S., & Sasselov, D. D. 2003, , 421, 507

Konacki, M., et al. 2004a, , 609, L37

Konacki, M., Torres, G., Sasselov, D. D. & Jha, S., 2004b, astro-ph/0412400, submitted to ApJL

Krisciunas, K., & Schaefer, B. E. 1991, , 103, 1033

Kron, R. G. 1980, , 43, 305

Lacy, C. H. 1977, , 218, 444

Landolt, A. U. 1992, , 104, 340

Lastennet, E., & Valls-Gabaud, D. 2002, , 396, 551

Le Fèvre, O. 2000, Astronomical Society of the Pacific Conference Series, 200, 47

Lipkin, Y., Leibowitz, E. M., Retter, A., & Shemmer, O. 2001, , 328, 1169

Maceroni, C., & Rucinski, S. M. 1999, , 118, 1819

Maoz, D., & Gal-Yam, A. 2004, , 347, 951

Matheson, T. et al. 2004, astro-ph/0411357, ApJ submitted

Mayor, M., & Queloz, D. 1995, , 378, 355

Mazeh, T., et al. 2000, , 532, L55

McGowan, K. E., & Charles, P. A. 2003, , 339, 748

Michel, P., Zappalà, V., Cellino, A., & Tanga, P. 2000, Icarus, 143, 421

Miknaitis, G., et al. 2004, American Astronomical Society Meeting Abstracts, 205,

Monet, D. B. A., et al. 1998, VizieR Online Data Catalog, 1252, 0

- Mushotzky, R. F., & Loewenstein, M. 1997, , 481, L63
- Ofek, E. O., & Maoz, D. 2003, , 594, 101
- Paczynski, B. 2001, *Astronomical Society of the Pacific Conference Series*, 246, 45
- Pont, F., Bouchy, F., Queloz, D., Santos, N. C., Melo, C., Mayor, M., & Udry, S. 2004, , 426, L15
- Pravdo, S. H., et al. 1999, , 117, 1616
- Rest, A., & SuperMacho Collaboration 2003, *American Astronomical Society Meeting Abstracts*, 203,
- Ricker, G. R., Vanderspek, R. K., & HETE Science Team 2003, *American Astronomical Society Meeting Abstracts*, 203,
- Sharon, K. et al., 2005, in preparation
- Smith, R. C., et al. 2002, *Bulletin of the American Astronomical Society*, 34, 1232
- Stokes, G. H., Evans, J. B., Viggh, H. E. M., Shelly, F. C., & Pearce, E. C. 2000, *Icarus*, 148, 21
- Stonebraker, M. & Rowe., L. A. 1986, "The Design of POSTGRES", *Proceedings of the ACM SIGMOD Conference*, Washington, DC, May, 1986.
- Strolger, L.-G., PANS, & GOODS 2004, *American Astronomical Society Meeting Abstracts*, 205,
- Tonry, J. L., et al. 2003, , 594, 1
- Tyson, J. A. 2002, , 4836, 10
- Udalski, A., Szymanski, M., Kaluzny, J., Kubiak, M., & Mateo, M. 1992, *Acta Astronomica*, 42, 253

- Udalski, A., Szymanski, M., Kaluzny, J., & Kubiak, M. 1994, *Acta Astronomica*, 44, 1
- Udalski, A., Szymanski, M., Kaluzny, J., Kubiak, M., Mateo, M., & Krzeminski, W. 1995, *Acta Astronomica*, 45, 237
- Udalski, A., Szymanski, M., Kaluzny, J., Kubiak, M., Mateo, M., Krzeminski, W., & Stanek, K. Z. 1997, *Acta Astronomica*, 47, 169
- Udalski, A., et al. 2002a, *Acta Astronomica*, 52, 1
- Udalski, A., Zebrun, K., Szymanski, M., Kubiak, M., Soszynski, I., Szewczyk, O., Wyrzykowski, L., & Pietrzynski, G. 2002b, *Acta Astronomica*, 52, 115
- Udalski, A., Szewczyk, O., Zebrun, K., Pietrzynski, G., Szymanski, M., Kubiak, M., Soszynski, I., & Wyrzykowski, L. 2002c, *Acta Astronomica*, 52, 317
- Udalski, A., Pietrzynski, G., Szymanski, M., Kubiak, M., Zebrun, K., Soszynski, I., Szewczyk, O., & Wyrzykowski, L. 2003, *Acta Astronomica*, 53, 133
- Udalski, A. 2003, *Acta Astronomica*, 53, 291
- Udalski, A., Szymanski, M. K., Kubiak, M., Pietrzynski, G., Soszynski, I., Zebrun, K., Szewczyk, O., & Wyrzykowski, L. 2004, *Acta Astronomica*, 54, 313
- Vanden Berk, D. E., et al. 2004, , 601, 692
- Vidal-Madjar, A., Lecavelier des Etangs, A., Désert, J.-M., Ballester, G. E., Ferlet, R., Hébrard, G., & Mayor, M. 2003, , 422, 143
- White, D. A. 2000, , 312, 663
- Wittman, D. M., et al. 2002, , 4836, 73
- Wolf, C., Wisotzki, L., Borch, A., Dye, S., Kleinheinrich, M., & Meisenheimer, K. 2003, , 408, 499

Wolszczan, A., & Frail, D. A. 1992, , 355, 145

York, D. G., et al. 2000, , 120, 1579

Appendix A

Table of Fields

For all the fields listed below we set: exposure time of 210 sec, Time_int_err=Time_int/3, and an airmass limit of 2.5.

<i>Field Name</i>	<i>R.A.</i>	<i>Dec.</i> [<i>days</i>]	<i>Time int.</i> [<i>hour</i>]	<i>H.A. Limit</i>	<i>Comments</i>
J0641+0928S	06:41:10.08	+09:28:37.2	1	4	KH15D
J1435+0008L	14:35:07.40	+00:08:53	4	2	
J1628+4348L	16:28:02.20	+43:48:33.3	15	1	
J1004+4112L	10:04:34	+41:12:40	1	3	
J0831+5215L	08:31:05.37	+52:15:20.4	15	1	B0827+525 (candidate) (offset 10min to south)
J0831+5245L	08:31:41.60	+52:45:17	15	1	B0827+525 (candidate) (offset 10min to south)
J0018+0256L	00:18:11.37	+02:56:39.4	15	1	LBQS0015+0239 (candidate)
J0025+1728L	00:25:37.09	+17:28:02.5	15	1	MG0023+171 (candidate)
J0105-2736L	01:05:34.74	-27:36:58.5	15	1	LBQS0103-2753 (candidate)
J0145-0945L	01:45:17.20	-09:45:12	15	1	Q0142-100
J0221+3556L	02:21:05.40	+35:56:13.8	15	1	B0218+357
J0232-2117L	02:32:33.10	-21:17:26	15	1	HE0230-2130
J0414+0534L	04:14:37.80	+05:34:42	15	1	MG0414+0534
J0438-1217L	04:38:14.90	-12:17:14.4	15	1	HE0435-1223
J0813+2545L	08:13:31.30	+25:45:03.2	15	1	HS0810+2554
J0821+1217L	08:21:39.10	+12:17:29	15	1	HS0818+1227
J0903+5028L	09:03:34.90	+50:28:19.5	15	1	SJ0903+50
J0911+0550L	09:11:27.50	+05:50:52	15	1	RXJ0911.4+0551
J0913+5259L	09:13:00.70	+52:59:31	15	1	SBS0909+532
J0921+4529L	09:21:12.80	+45:29:04.4	4	2	RXJ0921+4528
J0924+0219L	09:24:55.80	+02:19:24.5	15	1	SJ0924+0219
J0951+2635L	09:51:22.60	+26:35:14.1	15	1	FBQ0951+2635
J0955-0130L	09:55:00	-01:30:05	15	1	B0952-0115
J1012-0307L	10:12:15.80	-03:07:03	15	1	LBQS1009-0252
J1017-2047L	10:17:24.10	-20:47:00.4	15	1	Q1017-207
J1033+0711L	10:33:34.10	+07:11:25.5	15	1	B1030+074
J1106-1821L	11:06:33.70	-18:21:25	15	1	HE1104-1805

Continued on next page

<i>Field Name</i>	<i>R.A.</i>	<i>Dec.</i> [<i>days</i>]	<i>Time int.</i> [<i>hour</i>]	<i>H.A. Limit</i>	<i>Comments</i>
J1118+0745L	11:18:17	+07:45:59	15	1	PG1115+080
J1123+0137L	11:23:20.60	+01:37:48.5	15	1	Q1120+0195 (candidate)
J1131-1231L	11:31:51.60	-12:31:57	15	1	RXJ1131-12
J1155+1939L	11:55:18.30	+19:39:42	15	1	B1152+199
J1210+0954L	12:10:57.20	+09:54:25.6	15	1	1208+1011
J1216+5032L	12:16:13.40	+50:32:14	15	1	HS1216+5032 (candidate)
J1226-0054L	12:26:13.80	-00:54:56.8	15	1	SQJ1226-0054
J1335+0118L	13:35:34.79	+01:18:05.5	15	1	SJ1335+0133
J1355-2257L	13:55:43.38	-22:57:22.9	15	1	Q1355-2257
J1411+5211L	14:11:19.60	+52:11:29	15	1	HST14113+5211
J1415+1129L	14:15:46.40	+11:29:41.4	15	1	H1413+117
J1424+2256L	14:24:38.10	+22:56:00.6	15	1	B1422+231
J1432-0106L	14:32:29.07	-01:06:18	15	1	Q1429-008 (candidate)
J1521+5254L	15:21:44.80	+52:54:49	15	1	SBS1520+530
J1601+4316L	16:01:40.45	+43:16:47.8	15	1	B1600+434
J1633+3134L	16:33:48.90	+31:34:11	15	1	FBQ1633+3134
J1637+2636L	16:37:01.70	+26:36:06	15	1	Q1634+267 (candidate)
J1650+4251L	16:50:43.50	+42:51:45	15	1	SJ1650+4251
J1833-2103L	18:33:39.90	-21:03:40	15	1	PKS1830-211
J1934+5025L	19:34:30.95	+50:25:23.6	15	1	B1933+503
J2116+0225L	21:16:50.75	+02:25:46.9	15	1	B2114+022
J2152-2731L	21:52:07.40	-27:31:50	15	1	HE2149-2745
J2155-2041L	21:55:53.60	-20:41:45.2	15	1	LBQS2153-2056 (candidate)
J2240+0321L	22:40:30.30	+03:21:28.8	15	1	Q2237+0305
J2321+0527L	23:21:40.80	+05:27:36.4	15	1	B2319+052
J2348+0057L	23:48:19.60	+00:57:21.4	15	1	SQJ234819+0057 (candidate)
J1001+5027L	10:01:28.56	+50:27:57.6	2	4	SDSS1001+5027
J1206+4332L	12:06:29.76	+43:32:16.8	2	4	SDSS1206+4332
J0133+3023g	01:33:50.90	+30:23:25	5	1	M33 south
J0133+3055g	01:33:50.90	+30:55:49	5	1	M33 north
J0959+3044g	09:59:26.46	+30:44:47	5	1	Leo A NV=4
J1929-1740g	19:29:58.97	-17:40:41.3	5	1	Sgr Dwarf NV=0
J0000+0816C	00:00:10.56	+08:16:37.2	15	1	z=0.0396
J0011+3225C	00:11:47.04	+32:25:12	15	1	z=0.1073
J0020+2839C	00:20:31.92	+28:39:46.8	15	1	z=0.0955
J0021+2803C	00:21:37.68	+28:03:50.4	15	1	z=0.0943
J0040+0649C	00:40:00.48	+06:49:04.8	15	1	z=0.0395
J0040+2932C	00:40:29.52	+29:32:56.4	15	1	z=0.0712
J0041+2122C	00:41:46.56	+21:22:26.4	15	1	z=0.1014
J0043+2424C	00:43:52.08	+24:24:07.2	15	1	z=0.0830
J0049+2426C	00:49:48.48	+24:26:27.6	15	1	z=0.0815
J0058+2657C	00:58:55.44	+26:57:32.4	15	1	z=0.0470
J0107+3227C	01:07:28.32	+32:27:43.2	15	1	z=0.0170
J0108+0210C	01:08:09.60	+02:10:55.2	15	1	z=0.0447
J0113+1529C	01:13:01.20	+15:29:20.4	15	1	z=0.0442
J0115+0021C	01:15:08.88	+00:21:14.4	15	1	z=0.0448
J0123+3327C	01:23:12.24	+33:27:39.6	15	1	z=0.0146

Continued on next page

<i>Field Name</i>	<i>R.A.</i>	<i>Dec.</i> [<i>days</i>]	<i>Time int.</i> [<i>hour</i>]	<i>H.A. Limit</i>	<i>Comments</i>
J0123+3315C	01:23:41.04	+33:15:39.6	15	1	z=0.0164
J0125+0841C	01:25:03.84	+08:41:16.8	15	1	z=0.0491
J0125+0144C	01:25:24.72	+01:44:27.6	15	1	z=0.0181
J0152+3609C	01:52:45.84	+36:09:25.2	15	1	z=0.0163
J0155+3353C	01:55:03.84	+33:53:52.8	15	1	z=0.0872
J0228+2811C	02:28:16.56	+28:11:02.4	15	1	z=0.0350
J0246+3653C	02:46:08.16	+36:53:13.2	15	1	z=0.0488
J0257+0600C	02:57:38.88	+06:00:21.6	15	1	z=0.0238
J0257+1303C	02:57:49.68	+13:03:10.8	15	1	z=0.0722
J0258+1334C	02:58:56.88	+13:34:22.8	15	1	z=0.0739
J0338+0958C	03:38:42	+09:58:37.2	15	1	z=0.0349
J0341+1524C	03:41:22.08	+15:24:18	15	1	z=0.0290
J0352+1941C	03:52:59.76	+19:41:24	15	1	z=0.1090
J0413+1027C	04:13:26.16	+10:27:57.6	15	1	z=0.0882
J0419+0225C	04:19:38.64	+02:25:12	15	1	z=0.0123
J0459+0846C	04:59:11.28	+08:46:26.4	15	1	z=0.1000
J0503+0608C	05:03:06.48	+06:08:06	15	1	z=0.0880
J0716+5323C	07:16:36.96	+53:23:16.8	15	1	z=0.0644
J0751+5012C	07:51:22.08	+50:12:39.6	15	1	z=0.0220
J0753+2921C	07:53:24.24	+29:21:57.6	15	1	z=0.0621
J0759+5359C	07:59:40.56	+53:59:56.4	15	1	z=0.1038
J0823+0421C	08:23:11.52	+04:21:21.6	15	1	z=0.0293
J0828+3025C	08:28:40.80	+30:25:55.2	15	1	z=0.0503
J0912+1556C	09:12:29.76	+15:56:34.8	15	1	z=0.0851
J1002+3241C	10:02:37.68	+32:41:16.8	15	1	z=0.0500
J1053+5451C	10:53:47.76	+54:51:00	15	1	z=0.0704
J1109+2143C	11:09:27.12	+21:43:40.8	15	1	z=0.0319
J1110+2842C	11:10:46.80	+28:42:21.6	15	1	z=0.0314
J1111+4049C	11:11:28.56	+40:49:48	15	1	z=0.0794
J1123+1936C	11:23:12.96	+19:36:57.6	15	1	z=0.1042
J1134+4905C	11:34:59.52	+49:05:24	15	1	z=0.0338
J1143+4622C	11:43:40.08	+46:22:26.4	15	1	z=0.1167
J1144+1945C	11:44:36.48	+19:45:32.4	15	1	z=0.0214
J1204+0154C	12:04:27.36	+01:54:10.8	15	1	z=0.0200
J1205+3920C	12:05:11.76	+39:20:31.2	15	1	z=0.0370
J1206+2810C	12:06:35.28	+28:10:48	15	1	z=0.0283
J1210+0523C	12:10:17.04	+05:23:31.2	15	1	z=0.0770
J1217+0339C	12:17:41.28	+03:39:32.4	15	1	z=0.0750
J1223+1037C	12:23:05.76	+10:37:12	15	1	z=0.0257
J1230+1220C	12:30:47.28	+12:20:13.2	15	1	z=0.0036
J1241+1833C	12:41:18	+18:33:03.6	15	1	z=0.0718
J1259+2754C	12:59:31.92	+27:54:10.8	15	1	z=0.0231
J1303+1916C	13:03:44.88	+19:16:37.2	15	1	z=0.0634
J1320+3308C	13:20:08.40	+33:08:34.8	15	1	z=0.0362
J1326+0013C	13:26:18	+00:13:33.6	15	1	z=0.0820
J1341+2622C	13:41:50.40	+26:22:55.2	15	1	z=0.0724
J1342+0213C	13:42:06.72	+02:13:58.8	15	1	z=0.0776

Continued on next page

<i>Field Name</i>	<i>R.A.</i>	<i>Dec.</i> [<i>days</i>]	<i>Time int.</i> [<i>hour</i>]	<i>H.A. Limit</i>	<i>Comments</i>
J1348+2635C	13:48:52.32	+26:35:52.8	15	1	z=0.0622
J1349+2806C	13:49:27.60	+28:06:21.6	15	1	z=0.0748
J1353+0509C	13:53:06	+05:09:28.8	15	1	z=0.0790
J1359+2758C	13:59:12.48	+27:58:40.8	15	1	z=0.0612
J1413+4339C	14:13:43.68	+43:39:39.6	15	1	z=0.0890
J1421+4932C	14:21:36.24	+49:32:38.4	15	1	z=0.0710
J1431+2537C	14:31:03.60	+25:37:40.8	15	1	z=0.0908
J1440+0328C	14:40:37.44	+03:28:01.2	15	1	z=0.0276
J1442+2218C	14:42:17.52	+22:18:03.6	15	1	z=0.0970
J1452+1642C	14:52:59.52	+16:42:32.4	15	1	z=0.0444
J1454+1838C	14:54:30.96	+18:39:00	15	1	z=0.0586
J1510+3330C	15:10:10.80	+33:30:21.6	15	1	z=0.1130
J1510+0543C	15:10:54.96	+05:43:12	15	1	z=0.0766
J1511+0619C	15:11:23.52	+06:19:08.4	15	1	z=0.0817
J1516+0005C	15:16:16.32	+00:05:20.4	15	1	z=0.1183
J1516+0700C	15:16:42.24	+07:00:07.2	15	1	z=0.0353
J1518+0612C	15:18:41.28	+06:12:39.6	15	1	z=0.1021
J1520+4840C	15:20:53.04	+48:40:19.2	15	1	z=0.1076
J1521+3038C	15:21:17.04	+30:38:24	15	1	z=0.0777
J1522+0741C	15:22:01.68	+07:41:56.4	15	1	z=0.0453
J1522+2742C	15:22:26.88	+27:42:39.6	15	1	z=0.0723
J1523+0834C	15:23:01.68	+08:34:48	15	1	z=0.0355
J1524+2955C	15:24:09.84	+29:55:15.6	15	1	z=0.1145
J1539+2147C	15:39:38.40	+21:47:20.4	15	1	z=0.0411
J1539+3042C	15:39:48.48	+30:42:57.6	15	1	z=0.0980
J1540+1752C	15:40:09.12	+17:52:40.8	15	1	z=0.0916
J1545+3603C	15:45:00	+36:03:57.6	15	1	z=0.0654
J1558+2713C	15:58:22.08	+27:13:58.8	15	1	z=0.0894
J1602+1601C	16:02:18.72	+16:01:12	15	1	z=0.0353
J1604+1743C	16:04:42.96	+17:43:33.6	15	1	z=0.0370
J1604+2356C	16:04:57.12	+23:56:45.6	15	1	z=0.0318
J1620+2953C	16:20:30.72	+29:53:31.2	15	1	z=0.0972
J1628+3932C	16:28:39.60	+39:33:00	15	1	z=0.0299
J1657+2751C	16:57:51.36	+27:51:36	15	1	z=0.0347
J1659+3237C	16:59:44.16	+32:37:01.2	15	1	z=0.1013
J1702+3403C	17:02:40.08	+34:03:46.8	15	1	z=0.0970
J1709+3428C	17:09:48.48	+34:28:26.4	15	1	z=0.0802
J1733+4345C	17:33:01.20	+43:45:28.8	15	1	z=0.0330
J1740+3539C	17:40:31.92	+35:39:07.2	15	1	z=0.0430
J1744+3258C	17:44:13.44	+32:58:55.2	15	1	z=0.0757
J1810+4955C	18:10:50.40	+49:55:12	15	1	z=0.0473
J2114+0234C	21:14:06.24	+02:34:08.4	15	1	z=0.0483
J2214+1350C	22:14:47.76	+13:50:02.4	15	1	z=0.0263
J2226+1722C	22:26:02.64	+17:22:40.8	15	1	z=0.1072
J2235+0131C	22:35:40.32	+01:31:33.6	15	1	z=0.0591
J2250+1055C	22:50:17.04	+10:55:01.2	15	1	z=0.0768
J2310+0734C	23:10:30.96	+07:34:58.8	15	1	z=0.0400

Continued on next page

<i>Field Name</i>	<i>R.A.</i>	<i>Dec.</i> [<i>days</i>]	<i>Time int.</i> [<i>hour</i>]	<i>H.A. Limit</i>	<i>Comments</i>
J2317+1842C	23:17:50	+18:42:27	15	1	z=0.0422 & z=0.0389
J2323+1648C	23:23:53.52	+16:48:32.4	15	1	z=0.0416
J2324+1439C	23:24:20.16	+14:39:03.6	15	1	z=0.0428
J2335+2722C	23:35:05.04	+27:22:12	15	1	z=0.0613
J2336+2107C	23:36:34.08	+21:07:40.8	15	1	z=0.0565
J2338+2701C	23:38:27.60	+27:01:19.2	15	1	z=0.0309
J2344+0912C	23:44:56.88	+09:12:03.6	15	1	z=0.0400
J2350+2931C	23:50:34.56	+29:31:51.6	15	1	z=0.0950
J2350+0608C	23:50:51.12	+06:08:16.8	15	1	z=0.0562
J2355+1121C	23:55:50.88	+11:21:18	15	1	z=0.0720
J0519+1643v	05:19:24.43	+16:43:00.7	15	1	XXTau 18.5
J0528+3318v	05:28:34.05	+33:18:21.5	1	4	QZAur 18 b=-0.73 (Transit Field)
J0531+3026v	05:31:59.10	+30:26:45.2	1	4	TAur 15.2 b=-1.70 (Transit Field)
J0643-0201v	06:43:47.21	-02:01:13.7	1	4	BTMon 15.8 b=-2.62 (Transit Field)
J0644+2956v	06:44:12.05	+29:56:41.9	15	1	DMGem 16.7
J0654+3208v	06:54:54.37	+32:08:28.1	15	1	DNGem 15.8
J0726-0640v	07:26:47.06	-06:40:29.3	15	1	GIMon 18
J0803-2828v	08:03:22.80	-28:28:28.8	15	1	HZPup 18.5
J1545+1422v	15:45:39	+14:22:32.7	15	1	CTSer 16.6
J1619-0229v	16:19:17.60	-02:29:29.1	15	1	XSer 18.3
J1724-2436v	17:24:15.90	-24:36:50.2	15	1	V2109Oph 18
J1734-2810v	17:34:43.80	-28:10:35.8	15	1	V972Oph 16.6
J1738-2250v	17:38:49.20	-22:50:49.2	15	1	V794Oph 18
J1748-1845v	17:48:41.07	-18:45:37	15	1	V3888Sgr 16
J1750-2040v	17:50:23.50	-20:40:30.3	15	1	V1172Sgr 18
J1754-2614v	17:54:40.50	-26:14:15.2	15	1	V4643Sgr 16.
J1800-2733v	18:00:05.60	-27:33:14	15	1	V999Sgr 17.4
J1803-2800v	18:03:37.86	-28:00:08.5	15	1	V4579Sgr 16.5
J1814+1136v	18:14:07.17	+11:36:42.7	15	1	V849Oph 17
J1814+4151v	18:14:20.30	+41:51:21.3	15	1	V533Her 15
J1819-2511v	18:19:57.55	-25:11:14.7	15	1	V1016Sgr 17
J1821-2731v	18:21:40.47	-27:31:30	15	1	V4633Sgr 16.5
J1822-2534v	18:22:58.42	-25:34:47.1	15	1	GRSgr 16.6
J1826-2708v	18:26:46.62	-27:08:20	15	1	BSSgr 17
J1828-2134v	18:28:03.44	-21:34:24.7	15	1	HSSgr 16.5
J1830+0236v	18:30:46.92	+02:36:51.5	15	1	FHSer 16.2
J1835-1841v	18:35:49.21	-18:41:45.1	15	1	V3645Sgr 18
J1838-2322v	18:38:14.26	-23:22:47	15	1	V4021Sgr 18
J1843+1519v	18:43:42.59	+15:19:18.9	15	1	V827Her 18
J1846+1214v	18:46:31.48	+12:14:01.8	15	1	V838Her 18.3
J1853+2913v	18:53:24.97	+29:13:37.3	15	1	HR Lyr 15.8
J1855-0743v	18:55:26.70	-07:43:05.5	15	1	V373Sct 18.5
J1856-0412v	18:56:13	-04:12:32.7	15	1	EUSct 18
J1857+1314v	18:57:21.51	+13:14:29.9	15	1	V446Her 17.8

Continued on next page

<i>Field Name</i>	<i>R.A.</i>	<i>Dec.</i> [<i>days</i>]	<i>Time int.</i> [<i>hour</i>]	<i>H.A. Limit</i>	<i>Comments</i>
J1858-0524v	18:58:16.83	-05:24:05	15	1	FSSct 18
J1901-1309v	19:01:50.43	-13:09:42.5	15	1	V1059Sgr 18.1
J1917+0143v	19:17:13.53	+01:43:22.1	15	1	V356Aql 17.7
J1919+0037v	19:19:19	+00:37:53.7	15	1	V528Aql 18.1
J1920-0008v	19:20:24.30	-00:08:07	15	1	V606Aql 17.3
J1926+2721v	19:26:05	+27:21:58	15	1	PWVul 17.9
J1926+0736v	19:26:34.40	+07:36:13.6	15	1	V368Aql 15.4
J1929+2027v	19:29:14.60	+20:27:59.6	1	4	NQVul 18.5 b=+1.29 (Backup Transit Field)
J1931-0625v	19:31:25.80	-06:25:38.6	15	1	DOAql 16.5
J1948+2710v	19:48:00.50	+27:10:19.3	1	4	LVVul 16.9 b=+0.85 (Transit Field)
J1952+0828v	19:52:27.80	+08:28:46.4	15	1	V500Aql 17.8
J1952+3633v	19:52:37.60	+36:33:52.6	15	1	V465Cyg 17
J1958+5337v	19:58:24.60	+53:37:07.1	15	1	V476Cyg 17.2
J2052+3559v	20:52:44.70	+35:59:27	15	1	V1330Cyg 18.1
J2058+3556v	20:58:47.40	+35:56:27.9	15	1	V450Cyg 16.3
J2103+4845v	21:03:02	+48:45:52.9	1	4	V2275Cyg 18.8 b=+1.39 (Tran- sit Field)
J2111+4809v	21:11:36.60	+48:09:01.4	1	4	V1500Cyg 18.0 b=-0.07 (Tran- sit Field)
J2141+4250v	21:41:43.80	+42:50:28.3	15	1	QCyg 15.6
J2204+5330v	22:04:36.83	+53:30:23.7	15	1	IVCep 17.1
J2249+5317v	22:49:46.90	+53:17:18.3	15	1	DKLac 15.5
J2312+4728v	23:12:05.76	+47:28:19.7	15	1	OSAnd 18.4
J1425+3400D	14:25:12	+34:00:00	15	1	Bootes field
J1425+3430D	14:25:12	+34:30:00	15	1	
J1425+3500D	14:25:12	+35:00:00	15	1	
J1429+3400D	14:29:42	+34:00:00	15	1	
J1429+3430D	14:29:42	+34:30:00	15	1	
J1429+3500D	14:29:42	+35:00:00	15	1	
J1434+3400D	14:34:12	+34:00:00	15	1	
J1434+3430D	14:34:12	+34:30:00	15	1	
J1434+3500D	14:34:12	+35:00:00	15	1	
J0206-0500D	02:06:00	-05:00:00	15	1	Cetus field
J0206-0430D	02:06:00	-04:30:00	15	1	
J0206-0400D	02:06:00	-04:00:00	15	1	
J0210-0500D	02:10:30	-05:00:00	15	1	
J0210-0430D	02:10:30	-04:30:00	15	1	(Las Campanas IR survey)
J0210-0400D	02:10:30	-04:00:00	15	1	
J0215-0500D	02:15:00	-05:00:00	15	1	
J0215-0430D	02:15:00	-04:30:00	15	1	
J0215-0400D	02:15:00	-04:00:00	15	1	
J1324+2729D	13:24:21.40	+27:29:23	15	1	Subaru deep field
J2344+2700D	23:44:00	+27:00:00	15	1	FSVS F02
J2344+2730D	23:44:00	+27:30:00	15	1	FSVS F05
J0229+1445D	02:29:00	+14:45:00	15	1	FSVS F08

Continued on next page

<i>Field Name</i>	<i>R.A.</i>	<i>Dec.</i> [<i>days</i>]	<i>Time int.</i> [<i>hour</i>]	<i>H.A. Limit</i>	<i>Comments</i>
J0236+1518D	02:36:30	+15:18:00	15	1	FSVS F11
J0750+2048D	07:50:00	+20:48:00	15	1	FSVS F14
J1253+2620D	12:53:40	+26:20:00	15	1	FSVS F24
J1625+2633D	16:25:45	+26:33:50	15	1	FSVS F29
J0303+1938D	03:03:16	+19:38:11	15	1	FSVS F37
J1000+2039D	10:00:23	+20:39:11	15	1	FSVS F48
J1625+2703D	16:25:45	+27:03:48	15	1	FSVS F56
J0218-0700D	02:18:00	-07:00:00	15	1	CFHT legacy W1 (center)
J0854-0415D	08:54:00	-04:15:00	15	1	CFHT legacy W2/D2
J1417+5430D	14:17:54	+54:30:31	15	1	CFHT legacy W3 (center)
J0226-0430D	02:26:00	-04:30:00	15	1	CFHT legacy D1
J1419+5240D	14:19:28.01	+52:40:41	15	1	CFHT legacy D3
J2215-1744D	22:15:31.67	-17:44:05.7	15	1	CFHT legacy D4
J0332-2748D	03:32:25	-27:48:50	15	1	COMBO-17 / Chandra; (Las Campanas IR survey)
J0956-1001D	09:56:17	-10:01:25	15	1	COMBO-17 / A901
J1142-0142D	11:42:58	-01:42:50	15	1	COMBO-17 / S11
J0139-1011D	01:39:00	-10:11:00	15	1	COMBO-17 / A226
J1003+0154D	10:03:00	+01:54:00	15	1	VIRMOS VLT shallow (center, out of 2x2)
J1400+0500D	14:00:00	+05:00:00	15	1	VIRMOS VLT shallow (center, out of 2x2)
J2217+0024D	22:17:00	+00:24:00	15	1	VIRMOS VLT shallow (center, out of 2x2); SA22 (Las Campanas IR survey)
J0930-0000D	09:30:00	+00:00:00	15	1	Las Campanas IR survey
J1205-0727D	12:05:37	-07:27:29	15	1	Las Campanas IR survey; NTT Deep survey
J1524+0011D	15:24:54	+00:11:09	15	1	Las Campanas IR survey; IoA 1511
J2220-2440D	22:20:00	-24:40:00	15	1	Las Campanas IR survey; NICMOS 2220
J2138+0719D	21:38:00	+07:19:45	15	1	ALHAMBRA-1
J2343+1540D	23:43:30	+15:40:15	15	1	ALHAMBRA-2
J0334+5310X	03:34:59.90	+53:10:23	15	1	Porb=34.25 V=15.1 (HMXB)
J1909+0949X	19:09:37.90	+09:49:49	15	1	Porb=8.38 V=16.4 (HMXB)
J2032+3738X	20:32:15.30	+37:38:15	15	1	Porb=46.0 V=19.7 (HMXB)
J0044+3301X	00:44:50.40	+33:01:17	15	1	Porb=? V=19.3 (LMXB)
J0617+0908X	06:17:07.30	+09:08:13	15	1	Porb=? V=18.5 (LMXB)
J1605+2551X	16:05:45.80	+25:51:45	15	1	Porb=1.85 V=19.7 (LMXB)
J1858+2239X	18:58:41.58	+22:39:29.4	15	1	Porb=? V=15.3 (LMXB)
J1959+1142X	19:59:24	+11:42:30	15	1	Porb=9.33 V=18.7 (LMXB)
J2002+2514X	20:02:49.60	+25:14:12	15	1	Porb=8.26 V=18.9 (LMXB)
J2123-0547X	21:23:14.54	-05:47:52.9	15	1	Porb=5.96 V=16.8 (LMXB)
J2129+1210X	21:29:58.30	+12:10:03	15	1	Porb=17.1 V=15.8 (LMXB)
J2131+4717X	21:31:26.20	+47:17:24	15	1	Porb=5.24 V=16.4 (LMXB)

Appendix B

TAVAS Database Tables

B.1 Field Table

Field Table				
Column	Key	Type	Units	Description
FieldID	PF←	SERIAL UNIQUE NOT NULL		Field ID
FieldName		VARCHAR(11)		Field Name, format: <i>J#####±#####</i>
RA_Dec_field		POINT	deg	Field R.A.-Dec.
ExpTime		SMALLINT	sec	Typical Exposure Time; Default 210
Equinox_field		FLOAT	years	Coordinates equinox
Time_int		SMALLINT	days	Time interval between observations; Default 15
Time_int_Err		FLOAT	days	Time interval error
HA_Limit		SMALLINT	deg	Hour-angle limit; Default 15
AirMass_Limit		FLOAT		Airmass limit; Default 2.5
Target_RA_Dec		POINT	deg	Target R.A.-Dec.
AbsPhotZP		FLOAT	mag	Absolute photometric zero-point
Comments		VARCHAR(250)		

B.2 Image Table

Image Table				
Column	Key	Type	Units	Description
ImageID	PF <i>gets</i>	SERIAL UNIQUE NOT NULL		Image ID
ImageName	U	VARCHAR(30)		Image name, format: <i>YYYYMMDD.###</i> or <i>YYYYMMDD.J#####±#####.fits</i>

Continued on next page

Column	Key	Type	Units	Description
ImageType		VARCHAR(15)		CHECK: Science (Default) Bias Dark FF SkyFF DomeFF SuperFF Arc Lamp Standard Focus Calibration _link_ to Field.FieldID
FieldID	SF	INT NOT NULL		
NCombine		SMALLINT		CHECK: >0 Number of images combined (1-original image; ...)
JDMid	S	FLOAT	days	Julian Date
BJD		FLOAT	days	Barycentric JD
ExpTime		INT	sec	Exposure time CHECK: >=0
AirMass		FLOAT		Air mass
FilterID	F→	SMALLINT		_link_ to Filter.FilterID
Telescope	U	VARCHAR(8)		CHECK: 40 18 CONCAM WHAT
Instrument	U	VARCHAR(5)		CHECK: Cam MAALA FOSC
CCD	U	VARCHAR(4)		CHECK: SITe Tek ST10 ST8
Observer		VARCHAR(15)		Observer Name
Aper		VARCHAR(5)		Aperture wheel
Grism		VARCHAR(5)		Grism wheel
RotnAngl		FLOAT	deg	Rotator angle
PA		FLOAT	deg	Position Angle
Tmirror		FLOAT	°C	Mirror temperature
Tin		FLOAT	°C	Temperature inside dome
Tout		FLOAT	°C	Temperature outside dome
Hin		FLOAT	fraction	Relative humidity inside dome
Hout		FLOAT	fraction	Relative humidity outside dome
Press		FLOAT	mbar	Atmospheric pressure
WindAZ		FLOAT	deg	Azimuth of wind direction
WindSpeed		FLOAT	km/h	Wind speed
Clouds		FLOAT	fraction	Clouds coverage
RefImagePath		VARCHAR(100)		Path to reference image (not necessarily in Image_table)
HA_encoder		FLOAT	deg	H.A. from encoders
HA_Header		FLOAT	deg	H.A. from header
RA_Dec_encoder		POINT	deg	R.A.-Dec. from encoder
RA_Dec_Header		POINT	deg	R.A.-Dec. from header
UT		FLOAT	fraction	Standard time at beginning of exposure
ST		FLOAT	fraction	Local Sidereal Time
Gain		FLOAT	e ⁻ /ADU	CCD Gain
GainDL		FLOAT		CCD GainDL (for SITe CCD)
RDNoise		FLOAT	e ⁻	CCD ReadNoise
CRPIX1		FLOAT	pix	Image center X
CRPIX2		FLOAT	pix	Image center Y

Continued on next page

Column	Key	Type	Units	Description
CRVAL1_CRVAL2		POINT	deg	Image center R.A.-Dec. (assuming CTYPE1 is R.A., CTYPE2 is Dec.)
RA_rms		FLOAT	arcsec	Image astrometric STD in R.A. axis
Dec_rms		FLOAT	arcsec	Image astrometric STD in Dec. axis
Nast		SMALLINT		Number of astrometric reference stars used CHECK: >0
Naxis1		SMALLINT	pix	Image X axis size CHECK: >0
Naxis2		SMALLINT	pix	Image Y axis size CHECK: >0
CD1.1		FLOAT		Plate Scale solution
CD1.2		FLOAT		Plate Scale solution
CD2.1		FLOAT		Plate Scale solution
CD2.2		FLOAT		Plate Scale solution
NstarsInImage		INT		Number of stars found in image CHECK: >0
LimitingMag		FLOAT	mag	Instrumental limiting magnitude
Seeing		FLOAT	arcsec	Seeing at image center
MeanElongAtCenter		FLOAT		Mean elongation of stars at image center
USNO_PhotZP		FLOAT	mag	USNO E magnitude photometric zero point
PhotZP		FLOAT	mag	Relative photometry zero point
PhotZPdistortion		FLOAT[3x3]		PhotZP distortion matrix
ErrPhotZP		FLOAT	mag	Relative photometry error in zero-point
PhotZP_Chi2		FLOAT		Relative photometry Chi2 of zero-point
PhotZP_Dof		SMALLINT		Relative photometry Dof of zero-point CHECK: >0
Comments		VARCHAR(250)		

B.3 Filter Table

Filter Table				
Column	Key	Type	Units	Description
FilterID	PF←	SERIAL UNIQUE NOT NULL		Field ID
FilterName		VARCHAR(10)		Filter Name
Comments		VARCHAR(250)		

B.4 Object Table

Object Table				
Column	Key	Type	Units	Description
ObjectID	PF←	SERIAL UNIQUE NOT NULL		Object ID
FieldID	F→	SMALLINT		_link_ to Field.FieldID
RA_Dec_Mean	S	POINT	deg	Mean R.A.-Dec.
Epoch_Mean		FLOAT	years	Epoch of mean coordinates
RA_PM		FLOAT	arcsec/yr	Proper motion in RA
Dec_PM		FLOAT	arcsec/yr	Proper motion in Dec
RA_PM_Err		FLOAT	arcsec/yr	Error in RA proper motion
Dec_PM_Err		FLOAT	arcsec/yr	Error in Dec proper motion
PM_Chi2		FLOAT		Chi2 of PM fit
PM_Dof		SMALLINT		Dof of PM fit
DistBright		FLOAT	arcsec	Distance to nearest bright star
BrightMag		FLOAT	mag	Magnitude of nearest bright star
MeanMag		FLOAT	mag	Relatively calibrated weighted mean magnitude
StD		FLOAT	mag	StD of Relatively calibrated weighted mean magnitude
Chi2		FLOAT		Chi2 of calibrated weighted mean magnitude
Dof		SMALLINT		Dof of calibrated weighted mean magnitude CHECK: >=0
ObjectClass		INT		BIN CHECK: QSO CV lens Asteroid Kuiper SN None CHECK: >=0
USNO_E		FLOAT	mag	USNO E magnitude
USNO_O		FLOAT	mag	USNO O magnitude
USNO_Nstar		SMALLINT		Number of USNO stars within 1.5" from object CHECK: >=0
_2MASS_J		FLOAT	mag	2MASS J magnitude
_2MASS_H		FLOAT	mag	2MASS H magnitude
_2MASS_K		FLOAT	mag	2MASS K magnitude
_2MASS_Nstar		SMALLINT		Number of 2MASS stars within 1.5" from object CHECK: >=0
MeanX2overLocalMean		FLOAT	arcsec ²	Mean second moment over neighborhood second moment
MeanY2overLocalMean		FLOAT	arcsec ²	Mean second moment over neighborhood second moment

Continued on next page

Column	Key	Type	Units	Description
MeanXYoverLocalMean		FLOAT	arcsec ²	Mean second moment over neighborhood second moment
NsingleDet		SMALLINT		Number of detections of object in single images CHECK: >=0
NcombinedDet		SMALLINT		Number of detections of object in combined images CHECK: >=0

B.5 Phot Table

Phot Table				
Column	Key	Type	Units	Description
ObjectID	PF→	INT NOT NULL		Object ID
ImageID	PF→	INT NOT NULL		.link_ to Image.ImageID
RA_Dec	S	POINT	deg	Object R.A.-Dec. (per appearance) coordinates
X_Y		POINT	pix	Object X-Y coordinates
Mag4(instrumental)		SMALLINT	mag*1000	Object magnitude (aperture photometry 4")
Err4		SMALLINT	mag*1000	Object error magnitude (aperture photometry 4")
Mag6 (instrumental)		SMALLINT	mag*1000	Object magnitude (aperture photometry 6")
Err6		SMALLINT	mag*1000	Object error magnitude (aperture photometry 6")
Mag8 (instrumental)		SMALLINT	mag*1000	Object magnitude (aperture photometry 8")
Err8		SMALLINT	mag*1000	Object error magnitude (aperture photometry 8")
Mag_Auto (instrumental)		SMALLINT	mag*1000	Object magnitude (Auto photometry)
Err_Auto		SMALLINT	mag*1000	Object error magnitude (Auto photometry)
Mag_Iso (instrumental)		SMALLINT	mag*1000	Object magnitude (Iso photometry)
Err_Iso		SMALLINT	mag*1000	Object error magnitude (Iso photometry)
SubMag (instrumental)		SMALLINT	mag*1000	Object magnitude in subtracted image (aperture photometry)
SubErr		SMALLINT	mag*1000	Object error magnitude in subtracted image (aperture photometry)
DaoMag (instrumental)		SMALLINT	mag*1000	Object magnitude (daophot photometry)

Continued on next page

Column	Key	Type	Units	Description
DaoErr		SMALLINT	mag*1000	Object error magnitude (daophot photometry)
PeakVal		SMALLINT	counts	Peak value at non-bias non-FF image
X2		SMALLINT	pix ²	Object second moment (transformation: $X2(INT) = \log(X2(FLOAT)) \times 10,922 - 0.5$; to get log-precision from 1E-3 to 1E3)
Y2		SMALLINT	pix ²	Object second moment (transformation: $Y2(INT) = \log(Y2(FLOAT)) \times 10,922 - 0.5$; to get log-precision from 1E-3 to 1E3)
XY		SMALLINT	pix ²	Object second moment (transformation: $XY(INT) = XY(FLOAT) \times 3276.75 - 0.5$; to get precision from -10 to 10)
Saturation		BOOL		Object is at saturation level
Blend		BOOL		Object was originally blended
BadPix		BOOL		Object is nearby bad pixel
Confusion		BOOL		Nearby object less than ~ 1.5 , may be confused